CHALMERS
UNIVERSITY OF TECHNOLOGY

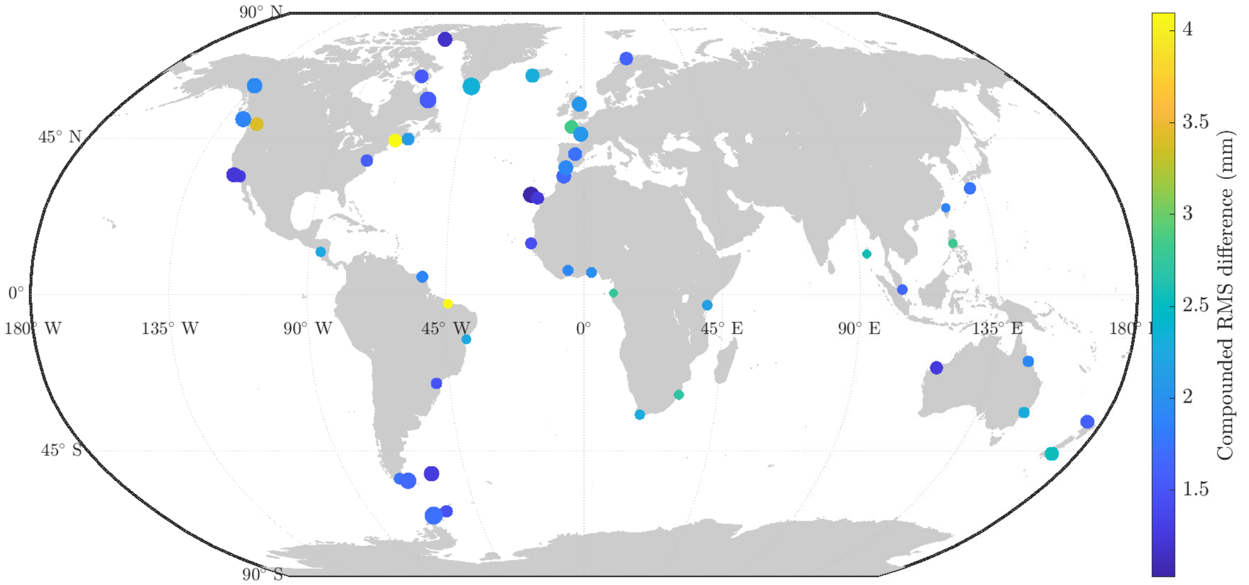

Observing ocean tidal loading with GNSS

Master's thesis in Physics and Astronomy

ANNA ANDERSSON

Department of Space, Earth and Environment
CHALMERS UNIVERSITY OF TECHNOLOGY
Gothenburg, Sweden 2020

Master's thesis 2020

Observing ocean tidal loading with GNSS

ANNA ANDERSSON

Department of Space, Earth and Environment
Onsala Space Observatory Division
Space Geodesy and Geodynamics research group
Chalmers University of Technology
Gothenburg, Sweden 2020

Observing ocean tidal loading with GNSS
ANNA ANDERSSON

Supervisors:
Jan Johansson, Department of Space, Earth and Environment
Maxime Mouyen, Department of Space, Earth and Environment
Hans-Georg Scherneck, Department of Space, Earth and Environment

Examiner:
Rüdiger Haas, Department of Space, Earth and Environment

Master's Thesis 2020
Department of Space, Earth and Environment
Onsala Space Observatory Division
Space Geodesy and Geodynamics research group
Chalmers University of Technology
SE-412 96 Gothenburg
Telephone +46 31 772 1000

Cover: The compounded RMS of the differences in ocean tidal loading between model FES2014b and GNSS observations for the M_2, N_2, O_1, Q_1 and M_f tidal constituents.

Typeset in LaTeX
Gothenburg, Sweden 2020

Observing ocean tidal loading with GNSS
ANNA ANDERSSON
Department of Space, Earth and Environment
Chalmers University of Technology

Abstract

Ocean tidal loading (OTL) is the displacement of the Earth's crust caused by the redistribution of sea water due to ocean tides. This affects geodetic measurements with Global Navigation Satellite Systems (GNSS), and can thus be observed with continuous GNSS measurements. OTL can also be modelled to remove its effect on geodetic measurements. This master thesis project aims to observe OTL with GNSS at 50 worldwide sites, and to compare these observations to four OTL models. Through investigation of disagreements between observations and models, insight into factors that negatively affect OTL models can be gained. The findings are similar in all four models. No clear, global geographical pattern was found, but there are indications of some geographical factors with negative effect on OTL models: inland sites and complex tidal conditions. It has been shown that three-year-long GNSS observations of OTL are accurate enough for use in evaluating OTL models. The disagreement between OTL models and observations is generally up to 2 mm in the radial component; larger differences indicate problems with models or observations. Observations of the solar tidal constituents proved problematic. The problem was identified as perturbing diurnal and semidiurnal signals, most likely solar driven perturbations, possibly in combination with multipath and monument stability issues. The tidal analysis method should be adjusted to eliminate these effects. There are also indications that GNSS observations of OTL are sensitive to Earth structure. It is thus possible that OTL observations with GNSS can be used to investigate Earth structure, and that Earth models can be adapted to improve OTL models.

Keywords: Ocean Tidal Loading (OTL), OTL model, Global Navigation Satellite Systems (GNSS), tidal analysis

Acknowledgements

I would like to thank my supervisors: Jan Johansson, Maxime Mouyen and Hans-Georg Scherneck, for the opportunity to work with them on this project. They have been exceedingly generous with their knowledge and advice, and I have learned so much from them.

Anna Andersson, Gothenburg, November 2020

Contents

1

Introduction

Ocean tides are caused by the gravitational pull of the Moon and Sun [1]. The redistribution of sea water due to ocean tides causes displacements of the Earth's crust, a geophysical phenomenon called ocean tidal loading (OTL) [2].

According to [3], ocean tides have been studied for a long time, and the connection to the Moon was made already by the Greek astronomer Pytheas in 330 B.C.E. Johannes Kepler supported this idea and suggested in 1609 that the tides were caused by a then unknown attractive force of the Moon and Sun. After Isaac Newton formulated the universal law of gravitation in 1687, he was able to mathematically describe the tides as the effect of gravitation. This discovery was built upon by Pierre de Laplace, who produced his tidal formula (1775), which describes the geographical distribution of tidal potential. In 1876, Lord Kelvin retracted his previous statement that the Earth was solid (but elastic), paving the way for the idea of an elastic Earth with a liquid core. After Charles Darwin's attempt to calculate the effect of the tides on this new Earth model (1882), he suggested the geophysical phenomenon known as ocean tidal loading.

Ocean tidal loading is of great interest because of the effect it has on geodetic and position measurements. The amplitude of ocean tidal loading varies with location, but the movements can be as large as several cm [4], and will affect position measurements with e.g. GNSS (Global Navigation Satellite Systems) and VLBI (Very Long Baseline Interferometry). This can of course be detrimental on occasions where very accurate measurements are needed, and is a problem.

The influence of ocean tidal loading on modern geodetic techniques can be dealt with following two different approaches. On one hand, continuous position measurements from GNSS [5] or VLBI [6] stations over several years can be analysed to extract the phase and amplitude of ocean tidal loading effects. According to [7], observation uncertainties of 0.2 mm should be achievable with 4 years of GNSS measurements with 70 % data availability. On the other hand, ocean tidal loading effects can be removed from the displacement time series, using ocean tidal loading predictions computed from ocean tide models. However, the models experience problems in certain conditions, with large ocean tide amplitudes in combination with shallow oceans and complex coastlines [8, 9]. Figure 1.1 shows an example of how large the change in ocean level can be; in some locations the ocean level can change several metres during the day.

Figure 1.1: *High and low tide in Brittany, France. Adapted from [8].*

The aim of this master's thesis is to observe ocean tidal loading with GNSS, and to compare the observations to model predictions. The intent is to characterise the differences between observations and models; the magnitude of the differences, the phase difference, the geographical distribution and the difference between constituents. This can provide insight into which factors have a detrimental effect on ocean tidal loading models.

For coastal sites, [9] show that the difference between models is on the millimetre level in the radial component for coastal sites, and at most 0.2 mm for inland sites. Thus, differences between models and observations are likely to also be of this magnitude. Larger differences might then indicate problems with loading models, or observations.

This report provides an overview of related theoretical concepts: ocean tidal loading and models thereof, and GNSS measurements. The methods employed within the project are explained, including the choice of sites for measurements, the acquisition and processing of GNSS data, tidal analysis of the resulting time series and finally the comparison between models and observations of ocean tidal loading. Since this is a master's thesis project, time is a limiting factor. For this reason, the number of sites has been limited to 50. This is because the processing of long time series of GNSS data takes a lot of time when using sub-daily time resolutions, which are needed for the tidal analysis of the time series.

After the theory and methods have been explained, the results of comparisons between models and observations as well as analysis of the observational data are presented. Possible implications on the models and the quality of the observations are discussed. The findings of this project are summarised in the conclusion.

2

Theory

This chapter describes the theoretical concepts used in this report. The first section details ocean tidal loading and how this phenomenon can be modelled. The second section explain the concept of GNSS.

2.1 Ocean tidal loading

The gravitational pull of the Sun and Moon on the Earth causes tidal motions of the solid Earth and the oceans [1]. In this report the focus is on ocean tides only. The redistribution of the ocean mass due to tides results in an elastic response of the Earth, causing periodic displacements (horizontal as well as vertical) of the Earth's crust [2]. This effect is called ocean tidal loading, and the displacements can be as large as several centimetres.

The rotation of the Earth and the movements of the Moon and Sun give rise to a wealth of tidal constituents, each characterised by a particular frequency. This is due to the different periodic effects in the movement of the Sun and the Moon, and the gravitational effects the Sun and Moon have on each other as well as on the Earth [1]. Ocean tides and therefore also ocean loading is the sum of of these constituents [1]. Table 2.1 lists examples out of all the numerous constituents that make up the total ocean tides on Earth. These are the constituents considered in this report.

It should be noted that according to International Earth Rotation and Reference System Service (IERS) conventions [10], 11 tide constituents are normally considered in ocean tidal loading. They are the constituents listed in Table 2.1 (except S_1) as well as the M_m (lunar monthly [11]) and S_{sa} (solar semiannual [11]) constituents. The last two constituent are not included in this report, as they would require longer time series to achieve an acceptable signal to noise ratio.

The periodic displacements due to ocean tidal loading effects contain the period, amplitude and phase of each tidal constituent. This can be observed in Figure 2.1a, which shows an example of a time series containing five days of data from the BRST GNSS station. Periodic signals are present in the time series at approximately diurnal and semidiurnal frequencies. The spectral density of a three year time series from the same site (which includes the five days in Figure 2.1a) is shown in Figure 2.1b. It displays several peaks; the frequencies of the peaks (e.g. at 2 cyc./d)

Table 2.1: *The 10 tidal constituents considered in this report [11]. (* = not normally included in ocean tidal loading, but used in this report to investigate perturbations.)*

Tidal constituent	Period (h)	
M_2	12.42	Principal lunar semidiurnal
S_2	12.0	Principal solar semidiurnal
N_2	12.66	Larger lunar elliptic semidiurnal
K_2	11.97	Lunisolar semidiurnal
K_1	23.93	Lunisolar diurnal
O_1	26.87	Lunar diurnal
P_1	24.07	Solar diurnal
Q_1	26.87	Larger lunar elliptic diurnal
M_f	327.86	Lunar fortnightly
S_1*	24.00	Solar diurnal

represents the periods of the different constituents of ocean tidal loading, and the relative amplitude of the constituents. The dotted red lines represent the M_2 and S_2 constituents.

The period of the ocean tidal loading effects remains the same as the period of the ocean tides, as the Earth's response to ocean tides is elastic [12]. Each constituent can therefore be identified in the spectral density of a time series such as the one in Figure 2.1b. The phase of each ocean tidal loading constituent can then be determined, and is measured in reference to the Greenwich prime meridian.

2.1.1 Models of ocean tidal loading

Ocean tidal loading can be modelled in order to estimate the effects in specific locations. This is necessary for the removal of ocean tidal loading effects from measurements of position over time with GNSS or VLBI [13], as these measurements are accurate enough that ocean tidal loading will affect the results. The displacement due to ocean tidal loading is computed by convolving a model for ocean tides with the theoretical Earth's surface displacement response to surface loading [1]:

$$u(r) = \rho \int_\Omega Z(r')G(|r - r'|)d\Omega. \tag{2.1}$$

Here, ρ is the mean density of sea water, $Z(r')$ is the height of ocean tide at r' given by the ocean tide model, and $G(|r-r'|)$ is a Green's function that describes the three dimensional displacement of the Earth as a response to a surface load. The integral is solved over the global surface of the Earth's oceans [14]. The displacement output by the model contains the amplitude and phase of each tidal constituent.

The Green's function $G(|r - r'|)$ that describes the Earth surface displacement is computed based on a theoretical model of the Earth, where the Earth is assumed to be Spherically symmetric, Non-Rotating, Elastic and Isotropic (SNREI model). The model commonly used is the Preliminary Reference Earth Model (PREM) [15]. An alternative is the Gutenberg-Bullen model [16, 17].

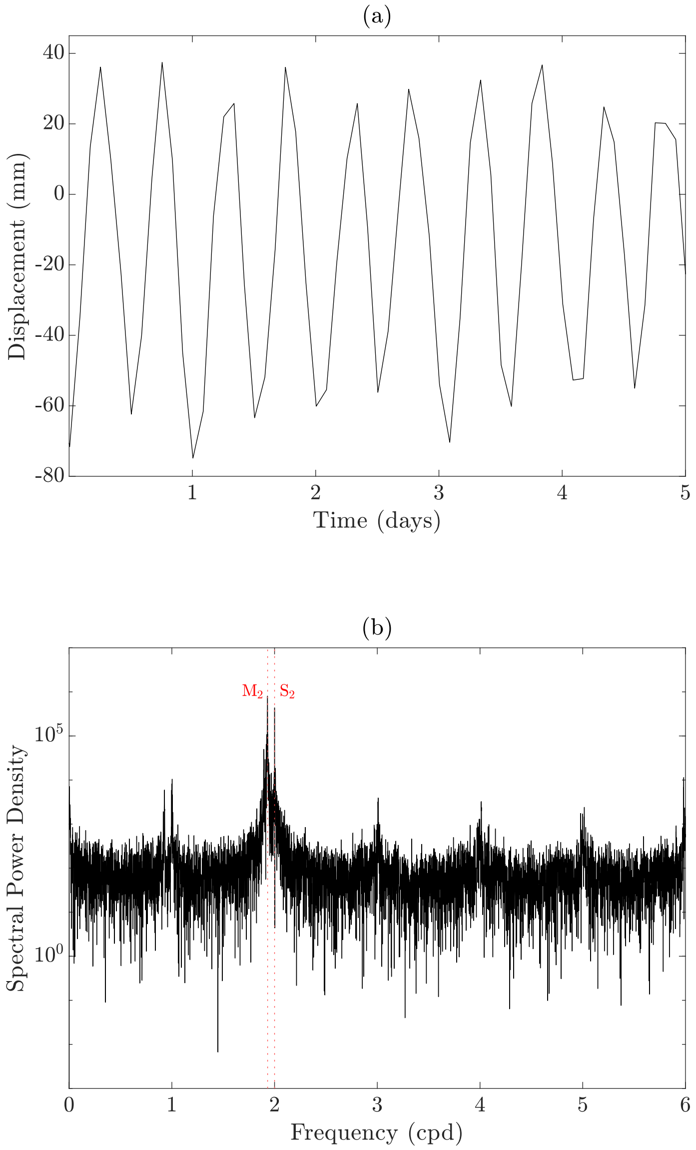

Figure 2.1: *Example of a time series containing a periodic signal caused by ocean loading. (a) shows the 5 day long time series. The spectral density of the time series is displayed in (b), and the peaks show the presence of several periodic signals, i.e. ocean loading constituents (the* M_2 *and* S_2 *constituents have been marked). The time series is the radial component of the GNSS station BRST, with a temporal resolution of 2 hours.*

Several models of ocean tides exist [18], with variable accuracy depending on the location where ocean tidal loading effects are to be estimated. As a result, the accuracy of the displacements due to ocean tidal loading estimated by models is limited primarily by the accuracy of the ocean tide models used for their computation [9]. This can prove to be a problem when estimating ocean tidal loading in several places, as the correctness of the results will differ between locations.

There are areas where problems arise in tide models. This includes areas with shallow sea depth and large tidal amplitudes. Figure 2.2 shows the geographical distribution of amplitudes and phases of the M2 tidal constituent. The English Channel and southern Argentina are examples of areas where the tidal amplitude is large. Because of the limited resolution of the tide models, areas with complicated coastlines are also problematic [9]. In ocean tidal loading models, the resolution of ocean tide models is decreased far from the location where the ocean loading is to be estimated [1]. This is done to save computation time. While the original, higher resolution is kept near the site in question, it is still low enough to cause problems.

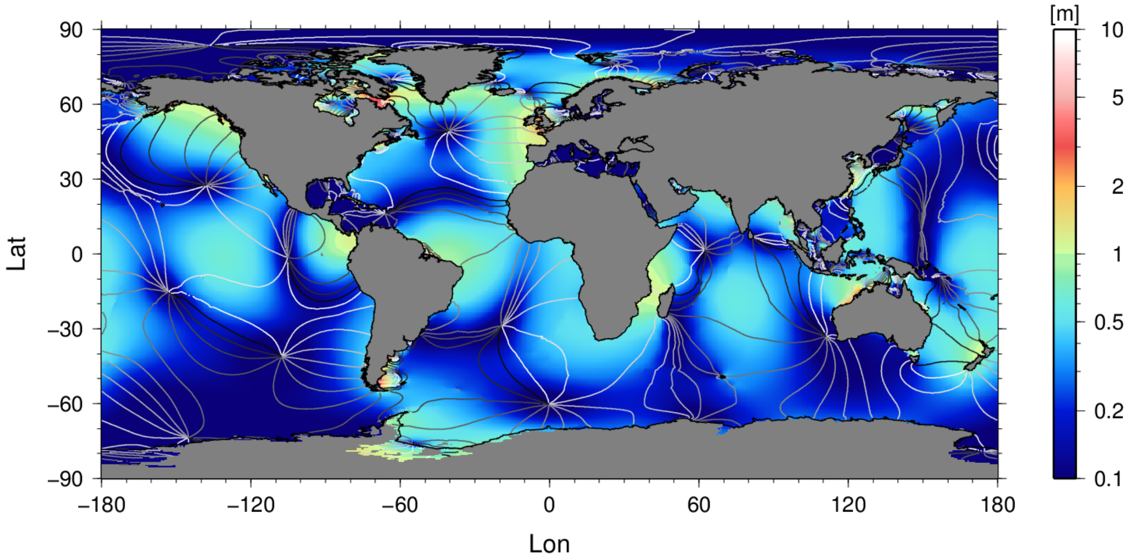

Figure 2.2: *The geographical distribution of amplitudes and phases of the M_2 tidal constituent. The colour scale shows amplitudes and the grey lines indicate phases in increments of 30° (0-330°) as the lines get darker. From [19].*

This report considers ocean tidal loading estimates based on four ocean tide models: FES2014b [20], TPX09-Atlas [21], HAMTIDE [22] and GOT4.10c [23]. The ocean tidal loading estimates are aquired from the ocean tidal loading provider in Onsala [24].

2.2 Global Navigation Satellite Systems (GNSS)

Global Navigation Satellite Systems (GNSS) is a system for determining positions on the Earth through trilateration between a ground-based receiver and several satellites orbiting the Earth. There are several variants of GNSS; the most commonly used is GPS (USA); other examples include GLONASS (Russia) and Galileo (EU). This section provides an overview of how GNSS works. Since this report uses only GPS data, specifics such as signals described here will be from the GPS system.

2.2.1 Satellites and receivers

GNSS is a system of satellites that orbit the Earth at a height of $\sim 20\,000$ km [25]. The satellites transmit signals that can be received by a receiver on Earth. For GPS, each satellite transmits two carrier signals: L_1 (1575 MHz) and L_2 (1228 MHz). The carrier signals are the same for every GPS satellite, but they are modulated by a C/A code (Carrier/Aquisition, public, 1.023 Mbit/s) and a P code (Precise, requires access, 10.23 Mbit/s) that allow a receiver to identify which satellite a signal is transmitted from [25]. The satellite signals also contain a data message, which provides the receiver with information about the satellite, such as the onboard atomic clock used to generate the signals, and the satellite orbit and health. The data message also contains information on other satellites in the system, as well as a model used by the receiver to correct errors in signal propagation caused by the atmosphere [25].

The satellites are monitored and controlled by ground based stations. These stations update the satellite data message with information on the orbits and clocks. The new information is based on observations and contains the parameters used to predict the orbit and clock behaviour of a satellite at a given moment [25].

The signal transmitted from a satellite is received by a GNSS receiver. The receiver generates its own version of the satellite signal, and the two signals are then correlated to find the difference in time (or phase) between the signals. This is the time it takes for the signal to travel from the satellite to the receiver [25, 26].

2.2.2 Position determination

The position of a receiver is determined by measuring the distance from the receiver to several satellites. This is done by determining the time $\Delta T = T^s - T_r$ that it takes a signal to travel from a satellite to the receiver through correlation, as mentioned above [27]. In theory, the distance to the satellite can then be calculated as $\Delta T \cdot c$, where c is the speed of light. In practise however, there are several problems. Firstly, the time T^s of the satellite and the time T_r of the receiver are not in the same time frame [27]. Secondly, both the satellite and receiver clocks contain errors that need to be accounted for [27]. Thirdly, the signal doesn't travel directly to the receiver at the speed of light, as there are errors due to atmospheric effects [26]. There is also noise which affects the results. Because of these problems, the distance that is measured by the receiver is called a pseudorange P_r^s, and contains all of the errors mentioned above [27]:

$$P_r^s = c(t^s - t_r) + c(\delta t^s - \delta t_r) + T_r^s + I_r^s + \nu_r^s, \tag{2.2}$$

Here, t^s and t_r are the times of the satellite and receiver in the same time frame, and δt^s and δt_r are the satellite and receiver clock errors, so that $T^s = t^s + \delta t^s$ and

$T_r = t_r + \delta t_r$. T_r^s and I_r^s are atmospheric effects (troposphere and ionosphere), and ν_r^s is noise. The true distance to the satellite is then

$$\rho = c(t^s - t_r) = \sqrt{(x^s - x_r)^2 + (y^s - y_r)^2 + (z^s - z_r)^2}, \tag{2.3}$$

where x^s, y^s, z^s is the position of the satellite, and x_r, y_r, z_r is the position of the receiver [27]. The position of the satellite is given by the satellite orbit information in the data message, and it remains then to determine the position of the receiver (x_r, y_r, z_r) as well as the satellite time in the receiver time frame, t^s. As there are four unknowns, measurements with at least four different satellites are required. The clock errors are provided by the data message and the receiver, and the atmospheric effects can be compensated for using the model provided by the data message. For higher accuracy however, it is possible to also determine the other error sources, e.g. T_r^s. This then requires the use of additional satellites [26].

Instead of measuring the time between satellite and receiver, the difference in signal phase can be measured. This has the potential to yield a more accurate position estimation [26]. The pseudorange then becomes [27]

$$P_r^s = \rho + c(\delta t^s - \delta t_r) + \lambda N + T_r^s - I_r^s + \nu_r^s. \tag{2.4}$$

This contains the additional term λN, which is the wavelength of the signal λ and the phase ambiguity N. The phase ambiguity is the number of complete phase cycles the signal makes while travelling between satellite and receiver. Note that this additional term increases the requirement on the number of satellite measurements needed for position determination. Note also that the ionosphere term (I_r^s) here is subtracted [26].

2.2.3 Accuracy of GNSS measurements

The accuracy of GNSS measurements is limited by a number of factors, such as the constellation of satellites available and the quality of the information in the data message. The use of the P code modulated carriers yields better results than the C/A code modulated carriers and as mentioned above, phase measurements increase the accuracy of measurements.

Post-processing of data can also increase the accuracy of GNSS measurements, as this allows for the use of after-the-fact information which is more accurate than for example the predictions of satellite orbits in the data message. The International GNSS Service (IGS) [28] provides information about the satellite orbits and clocks, and the International Earth Rotation and Reference Systems Service (IERS) [29] provides information on Earth orientation parameters and tidal movements. This is necessary in order to convert measurements from a celestial coordinate system to an Earth coordinate system, and to remove tidal effects from measurements. Additional information like antenna calibration and atmospheric conditions at the station is also used.

In this report, data from stationary GNSS receivers is used in post-processing, and the accuracy can be expected to be a few mm [26, 27]. Note that GNSS measurements generally have lower accuracy in the height component than in the horizontal components due to the satellite constellations.

3

Methods

This chapter describes the methods used in measuring ocean tidal loading, and comparing the observations with existing ocean tidal loading models. In the first section, the process of choosing GNSS stations and aquiring data is explained. Thereafter, the GNSS data processing is described, followed by the tidal analysis procedure. Finally, the models and method of model data acquisition is presented, along with an explanation of how the comparison was performed.

3.1 Choice of GNSS stations and aquisition of data

A total of 50 GNSS stations from the IGS network were chosen based on five criteria:

1. Within 50 km of the closest coastline.
2. Large amplitude in M_2 tidal constituent (40 stations) and O_1 tidal constituent (10 stations).
3. Good spread over the world, particularly in problematic areas for ocean loading models: e.g. Indonesia, southern Argentina, Iceland.
4. At least 3 years of good quality data available (see Figure 3.1 for an example of good/bad data):
    - No jumps.
    - Low standard deviation.
    - Avoid gaps where possible.
5. Where possible, more recent data has priority.

The criteria were implemented in the following way: A list of the GNSS stations in the IGS network in locations no further than 50 km from the coast was assembled, together with the theoretical amplitudes of the M_2 and O_1 tidal constituents at each station, based on the FES2014b tide model. This was done in order to identify sites where the tidal amplitudes are larger and where the ocean tidal loading displacements can be measured. The time series' and residuals for the stations were downloaded from [30]. The residuals were analysed to find the mean and time-dependent standard deviation, and the time series were analysed to find jumps or gaps. In total, 50 stations and time frames (40 from the M_2 constituent list and 10 from the O_1 constituent list) were chosen, with regard to the data quality and achieving a good spread over the world and in key locations.

Figure 3.1 shows examples of time series for two of the considered stations. The MAG0 time series contains frequent jumps (examples indicated by red circles), while the YEBE time series lacks these features. The MAG0 station was excluded for use in this report, while the good data quality of the YEBE station made it more suitable for ocean tidal loading measurements.

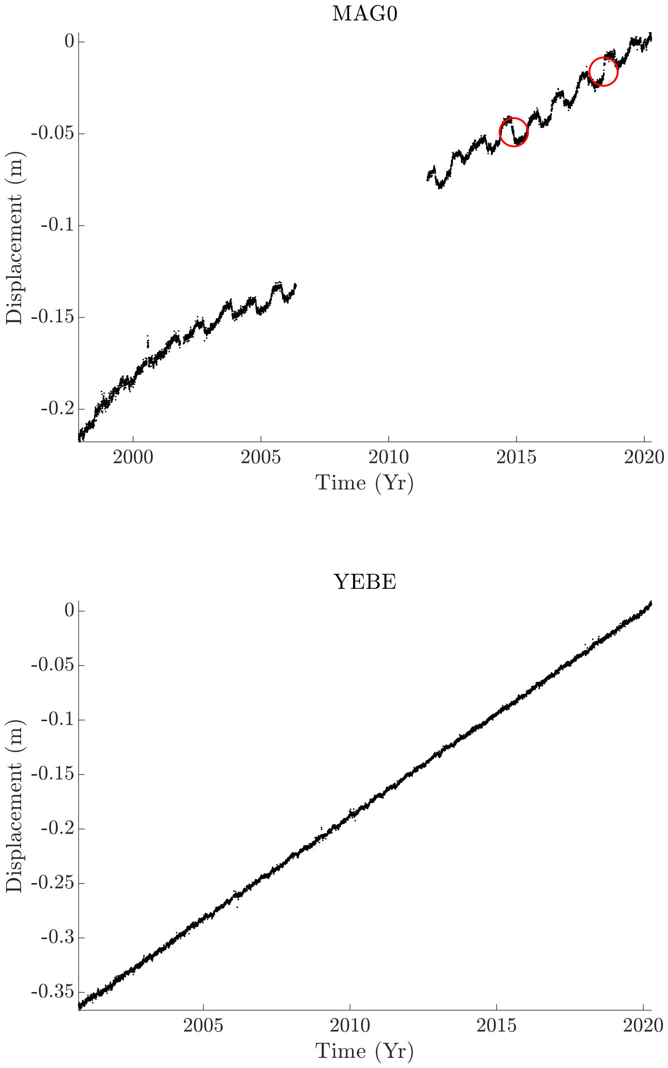

Figure 3.1: *Time series from GNSS stations MAG0 and YEBE. The MAG0 time series contains many jumps (two examples indicated by red circles). It is therefore unsuitable for ocean tidal loading measurements. The YEBE time series contains no such jumps however, and was therefore one of the chosen stations with good data quality.*

The chosen stations, their coordinates and the time frame used are given in Table A.1. Figures 3.2, 3.3, 3.4 and 3.5 show the locations of the stations. The GNSS data from these stations was acquired from the International GNSS Service [28].

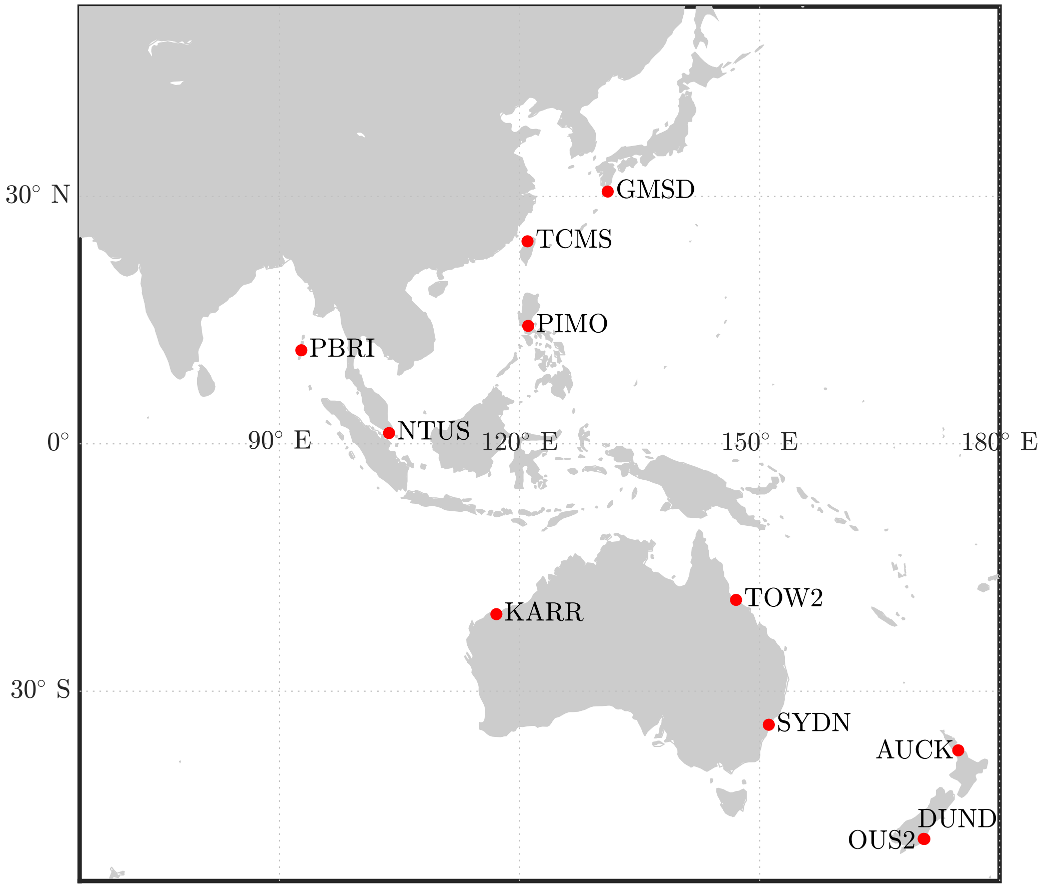

Figure 3.2: *Map of the GNSS stations in Asia and Oceania used in this report.*

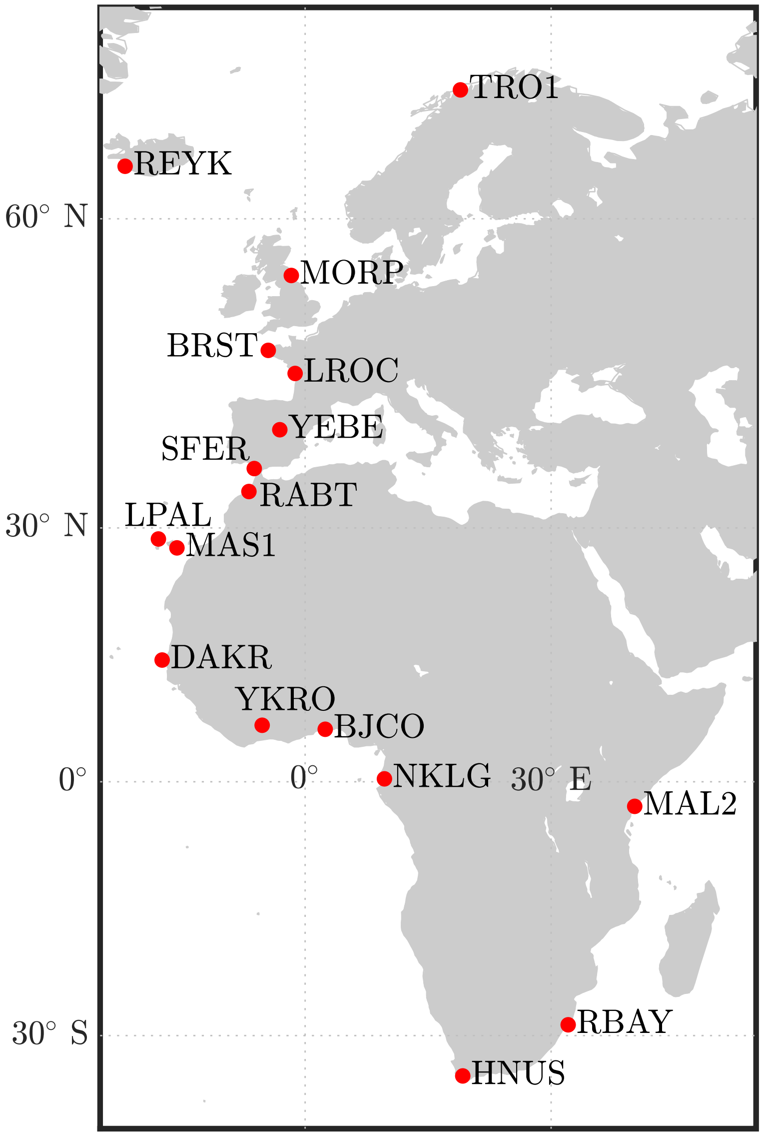

Figure 3.3: *Map of the GNSS stations in Europe and Africa used in this report.*

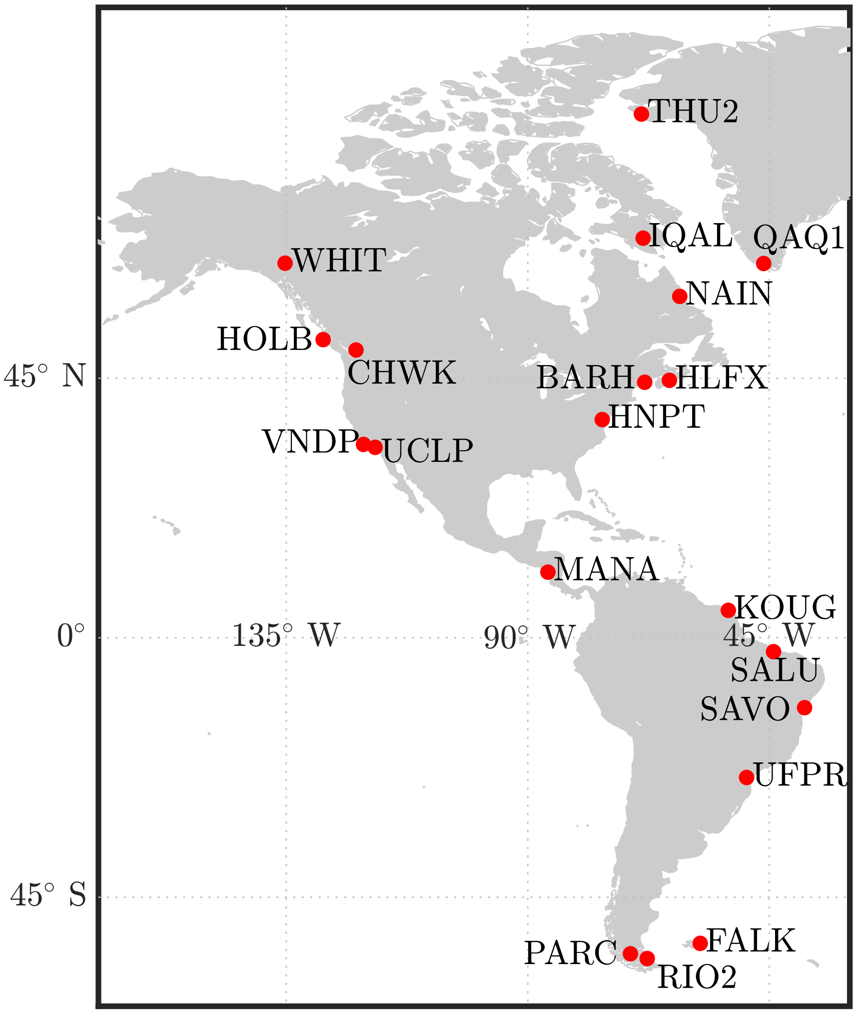

Figure 3.4: *Map of the GNSS stations in North and South America used in this report.*

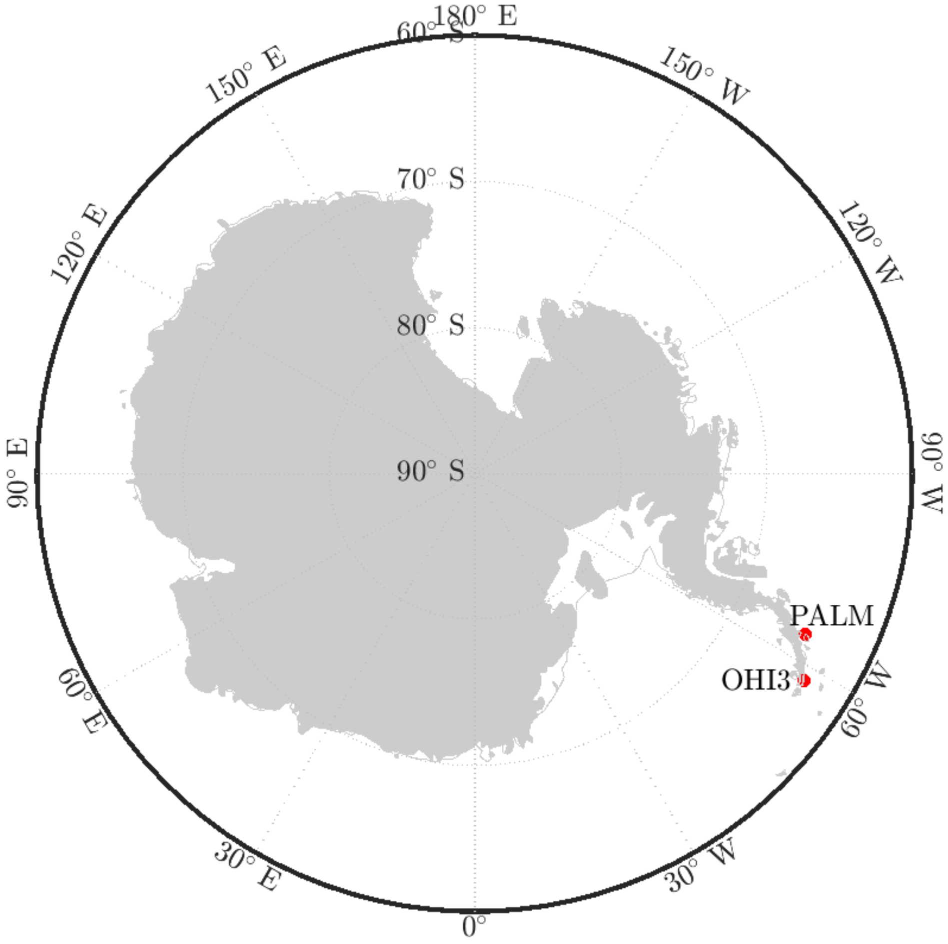

Figure 3.5: *Map of the GNSS stations in Antarctica used in this report.*

3.2 GNSS data processing

GIPSY-OASIS (hereinafter referred to as GIPSY) is a software for processing raw GNSS data [31]. There are two types of GNSS data processing softwares: precise positioning-based and differentiating-based softwares. GIPSY is an example of the former, which yields accurate results while processing large amount of data at a fast rate [32]. In this project, GIPSY-OASIS v6.2 was used for the GNSS data processing, and only GPS data was included in the analysis.

The flowchart in Figure 3.6 describes the working process of GIPSY.

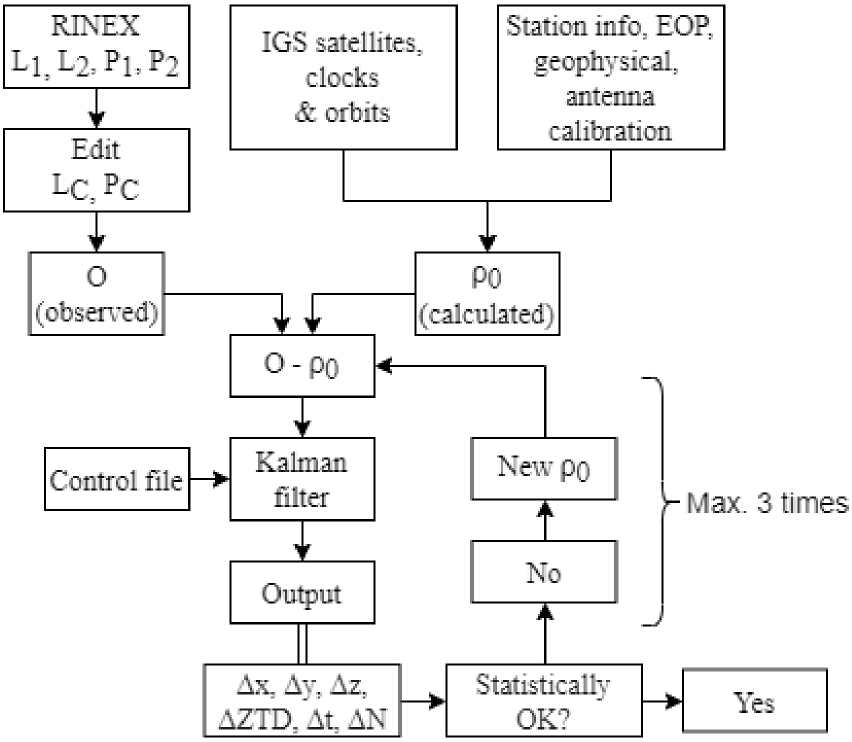

Figure 3.6: *The working process of GIPSY.*

GNSS stations generate RINEX files, which is a standardised format that allows data from different types of stations to be used together, and is the input format for GIPSY [33]. In Figure 3.6 L_1, L_2, P_1 and P_2 are the two C/A and P code modulated carrier signals. The sampling rate is usually 30 s.

In the editing phase of GIPSY, only data with a sampling rate of 5 min is kept while the rest is discarded. This is done to shorten the processing time. GIPSY also eliminates data segments that are too short (< 30 min), as too many short solutions lower the quality of the phase ambiguity solutions. Finally, ionospheric effects are (mostly) removed by creating linear combinations of the two carrier signals, for the

C/A and P code respectively[34]:

$$L_c = \frac{f_{L_1}^2}{f_{L_1}^2 - f_{L_2}^2}\mathrm{L}_1 - \frac{f_{L_2}^2}{f_{L_1}^2 - f_{L_2}^2}\mathrm{L}_2 = 2.546\ \mathrm{L}_1 - 1.546\ \mathrm{L}_2 \tag{3.1}$$

$$P_c = \frac{f_{P_1}^2}{f_{P_1}^2 - f_{P_2}^2}\mathrm{P}_1 - \frac{f_{P_2}^2}{f_{P_1}^2 - f_{P_2}^2}\mathrm{P}_2 = 2.546\ \mathrm{P}_1 - 1.546\ \mathrm{P}_2 \tag{3.2}$$

L_c and P_c form the observable O.

GIPSY also computes a range ρ_0 based on a number of parameters input by the user [35]. This includes satellite orbit and clock parameters, Earth orientation parameters, geophysical information (e.g. tides, ocean tidal loading), antenna calibration and station information (e.g. tropospheric delay). For this project, the tropospheric estimation parameter was set to 10^{-5} km/$\sqrt{\mathrm{h}}$, and the VMF1 [36] tropospheric mapping function was used. The tropospheric gradient was not estimated (see Appendix B). Fiducial orbit and clock parameters flinnR [37] were used. The tide models used for corrections in this project were WahrK1 and FreqDepLove (solid Earth tide), PolTid (polar tide) and OctTid [38]. Ocean tidal loading effects were not input, as they were to be measured. Note that atmospheric loading was not accounted for in the geophysical models input into GIPSY, so the resulting time series will include these effects.

The observed range O and the computed range ρ_0 are compared in an LSQ-based Kalman filter [35]. The Kalman filter iteratively tries to estimate the range within the constraints given by the control file. The statistical validity of the solution given by the Kalman filter is examined, and if the solution is deemed poor, it is input into the Kalman filter again as a new computed range ρ_0. This re-iteration can be performed at most 3 times, after which GIPSY discards that particular time series [35]. In this project, the statistical settings used were as follows: The apriori position σ 10^{-4} km was used, and the process σ was set to 10^{-6} km/$\sqrt{h}$. The noise model RANDOM WALK was used. The posterior statistical error margin was set to 5 m for code measurements, and 2.5 cm for phase measurements.

An advantage of post-processing with GIPSY is that the Kalman filter can run the data forwards as well as backwards, which means the solution for a data point in the time series can be adjusted with respect not only to previous data points, but also later data points. This increases the plausibility of the solution.

The time resolution of the positions calculated by GIPSY was set to be 2 h (see Appendix B), as sub-daily time resolution is needed to accurately sample tides at diurnal and semidiurnal frequencies. Kinematic settings were used and continuous periodic motions were expected. The minimum elevation limit for the GNSS satellites was set to 10°. To achieve the low uncertainty needed to measure ocean tidal loading effects, integer phase ambiguity resolution [39] was used.

GIPSY processing is usually done with 24 h of data at a time, regardless of the time resolution of the positions output by GIPSY. Because of this, positions from the beginning of each day might exhibit larger variations where the position estimates calculated by GIPSY have not yet stabilised. When longer time series are put together using several days' data, a 24 h periodic pattern will then occur. This can interfere with the tidal analysis of ocean tidal loading effects in *urtapt*. To alleviate this problem, a total of 30 h of GNSS data were used when processing each day in GIPSY - the 24 h of the day in question and the 3 h preceding and succeeding that day. These preceding and succeeding hours were then discarded when assembling the three-year time series.

3.3 Tidal analysis

Tidal analysis attempts to extract a defined set of tidal constituents at different frequencies from a time series obtained e.g. through processing of GNSS data (see Section 3.2). The tidal analysis returns the amplitude and phase of each of these constituents. In this project the software *urtapt* [40] was used for tidal analysis of the time series output by GIPSY to characterise ocean tidal loading effects at the selected sites.

urtapt uses a weighted least-square based method with generalised inverse to fit model signals to the periodic signals in data. The weights are based on the uncertainties of the input data; in this report the input data was the GNSS data processed with GIPSY, and the uncertainties used as weights were provided by GIPSY.

Data input to *urtapt* is decorrelated with a prediction error filter (PEF) to fulfil the least-squares requirement of uncorrelated errors [41]. As the order of the filters is finite, breaks appear in the sampled data. The PEF's used in *urtapt* are of relatively low order, which reduces the length of the breaks. In this project, the order of the PEF was set to 9, 15, 25 or 50; see Table C.1 for the PEF orders used for each station. Section B.1 in Appendix B explains how the optimal order of the PEF was determined using a maximum entropy approach.

urtapt provides the option to estimate features in data which might prove problematic in the tidal analysis. This includes long-time trends like tectonic plate motion and isostatic adjustment, as well as more short-term problems like jumps. A synthetic signal is generated based on these features, and the effects are removed from the analysis. This option was used to eliminate effects from tectonic plate motion and isostatic uplift, but as no jumps were apparently present in the data (determined from GNSS time series from [30]), this was not accounted for in the analysis.

It is possible to add ancillary observational data to remove effects of other phenomena that could affect the tidal analysis. An example of a phenomenon that can affect analysis of ocean tidal loading is atmospheric loading. The ancillary data could then consist of air pressure data and corresponding Earth crustal displacement models. No ancillary data was used for this project. Although atmospheric loading most likely has an effect on the results as this is not compensated for in the GNSS processing, the effect is too small for ancillary data to be useful with the current uncertainty of the GNSS measurements used [42].

After the tidal analysis, the amplitude, cophase and amplitude uncertainty σ_{amp} were collected from the *urtapt* results, and the phase uncertainty σ_{phase} was calculated according to the following equation:

$$\sigma_{\text{phase}} = \arcsin\left(\frac{\sigma_{\text{amp}}}{\text{amplitude}}\right) \cdot \frac{180^\circ}{\pi} \tag{3.3}$$

The observed phases output from *urtapt* turned out wrong due to an error in the time stamps of the time series used; the difference between the time stamps and the correct time was 1 h, and so the correct phases θ_{obs} were calculated as follows:

$$\theta_{\text{obs}} = \theta'_{\text{obs}} - f \cdot \Delta t. \tag{3.4}$$

Here θ'_{obs} is the observed (incorrect) phase, f is the frequency and $\Delta t = 1$ h (the delay in the time stamps).

3.4 Ocean tidal loading model acquisition

Ocean tidal model estimations for the positions of all 50 stations were acquired from [24]. Four tide models were used: FES2014b [20], TPX09-Atlas [21], HAMTIDE [22] and GOT4.10c [23]. Estimations from all models were acquired with centre of motion correction (CMC; Appendix B.3 compares results with and without CMC corrections), and an elastic Green's function was chosen. Note that requests for the FES2014b and TPXO9-Atlas tide models were forwarded to SEGAL [43]. Therefore the HAMTIDE and GOT4.10c ocean tidal loading estimations were calculated with the Gutenberg-Bullen Earth model, while the FES2014b and TPXO9-Atlas estimations were calculated with the PREM Earth model.

3.5 Comparison between observations and models

The difference between model estimations and observed effects was calculated using Matlab. This was done for the amplitude and cophase of each tidal constituent.

Ocean tidal loading observations are divided into three components; the **R** or **radial component** is oriented radially with the positive direction upwards; the **E** or **east component** is oriented east-west, positive in the east direction; the **N** or **north component** is oriented north-south, positive in the north direction.

As the phases output by urtapt and OTL were defined differently in the east-west and north-south directions, the horizontal components of the model phases were corrected according to the definitions used in observed phases:

$$\theta_{\text{mod}} = \theta'_{\text{mod}} + \gamma \cdot 180^\circ, \qquad \gamma = \begin{cases} 1, & \text{for horizontal components.} \\ 0, & \text{otherwise.} \end{cases} \tag{3.5}$$

where θ_{mod} is the corrected phase. The negative of the observed phase ($-\theta_{\text{obs}}$) was also used for the same purpose.

Figure 3.7 shows an example of an ocean tidal loading observation (red) and model prediction (blue) displayed as phasors in a complex plane ($\mathrm{P_{obs}}$ and $\mathrm{P_{mod}}$, respectively). The difference between observation and model is displayed in black ($\mathrm{P_{diff}} = \mathrm{P_{obs}} - \mathrm{P_{mod}}$). The **uncertainty** is the standard deviation σ_{amp} of the observed ocean loading amplitude. This is displayed in Figure 3.7 as a dotted red circle around the observation phasor.

The following quantities were also calculated:

The **amplitude of the (phasor) difference** is the length of the phasor difference ($|\mathrm{P_{diff}}|$). The **phase difference** is the difference between the phases ($\theta_{\mathrm{diff}} = |\theta_{\mathrm{mod}} - \theta_{\mathrm{obs}}|$), *not* the phase of the phasor difference.

The **absolute difference** refers to the amplitude of the (phasor) difference between model and observation phasors, divided by the uncertainty ($\frac{|\mathrm{P_{diff}}|}{\sigma_{\mathrm{amp}}}$).

The **relative difference** is the amplitude of the phasor difference divided by the amplitude of the model phasor ($\frac{|\mathrm{P_{diff}}|}{|\mathrm{P_{mod}}|}$).

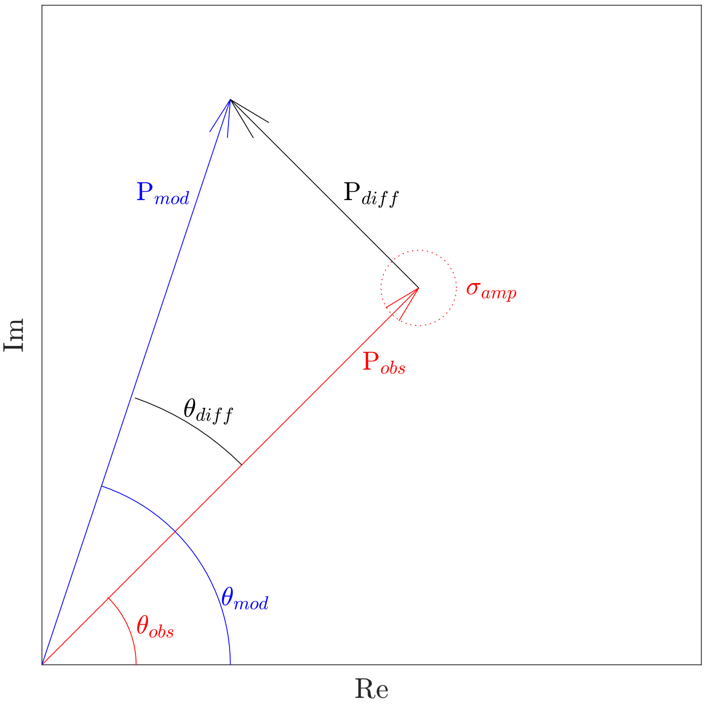

Figure 3.7: *Example of an ocean tidal loading observation (red) and model prediction (blue) displayed as phasors in a complex plane (P_{obs} and P_{mod}, respectively). The difference between observation and model is displayed in black ($P_{diff} = P_{obs} - P_{mod}$). The dotted ring denotes the observation uncertainty σ_{amp}.*

4

Results

The amplitude and phase of ocean tidal loading for nine tidal constituents at 50 sites spread over the world has been observed using GNSS stations, as described in Sections 3.1 (Stations choice and data aquisition), 3.2 (GNSS data processing) and 3.3 (Tidal analysis of time series). Model predictions of ocean tidal loading at the same 50 sites have been acquired (see Section 3.5). A complete list of the sites can be found in Table A.1, and the location of the sites is marked on the maps in Figures 3.2, 3.3, 3.4 and 3.5. The model predictions are based on four different ocean models: FES2014b [20], TPX09-Atlas [21], HAMTIDE [22] and GOT4.10c [23]. Table 2.1 contains a list of the nine tidal constituents considered, their periods and their classifications.

This chapter compares these observations and model predictions. The first sections show that the results are similar between the different ocean models. The second section covers the geographical aspects of model - observation differences. This is followed by a more detailed investigation into the differences between model and observations in the different tidal constituents. After this, the presence of perturbing signals at diurnal and semidiurnal frequencies is shown. Finally, the occurrence of pairing of the models in the O_1 constituent is examined. For an explanation of the quantities used, see Section 3.5.

As the results are similar between the different ocean models, the main focus of this chapter is on the FES2014b model. A table of the observed ocean tidal loading data for the M_2 and O_1 constituents can be found in Appendix D.

4.1 Model differences

The mean difference between model and observations of ocean tidal loading seen is very similar in all four models (FES2014b, GOT4.10c, HAMTIDE, TPX09-Atlas). Figure 4.1 shows this mean difference between model and observations for each model and constituent in all components. The error bars depict the standard deviation of the differences, σ_{diff}. The standard deviation is quite large, owing to the great geographical variation in loading amplitude, but for all constituents and in all components, the compounded differences for each model are within $1 \cdot \sigma_{\text{diff}}$ of each other. Thus, in the following sections the focus is on the FES2014b model, with the exception of last section.

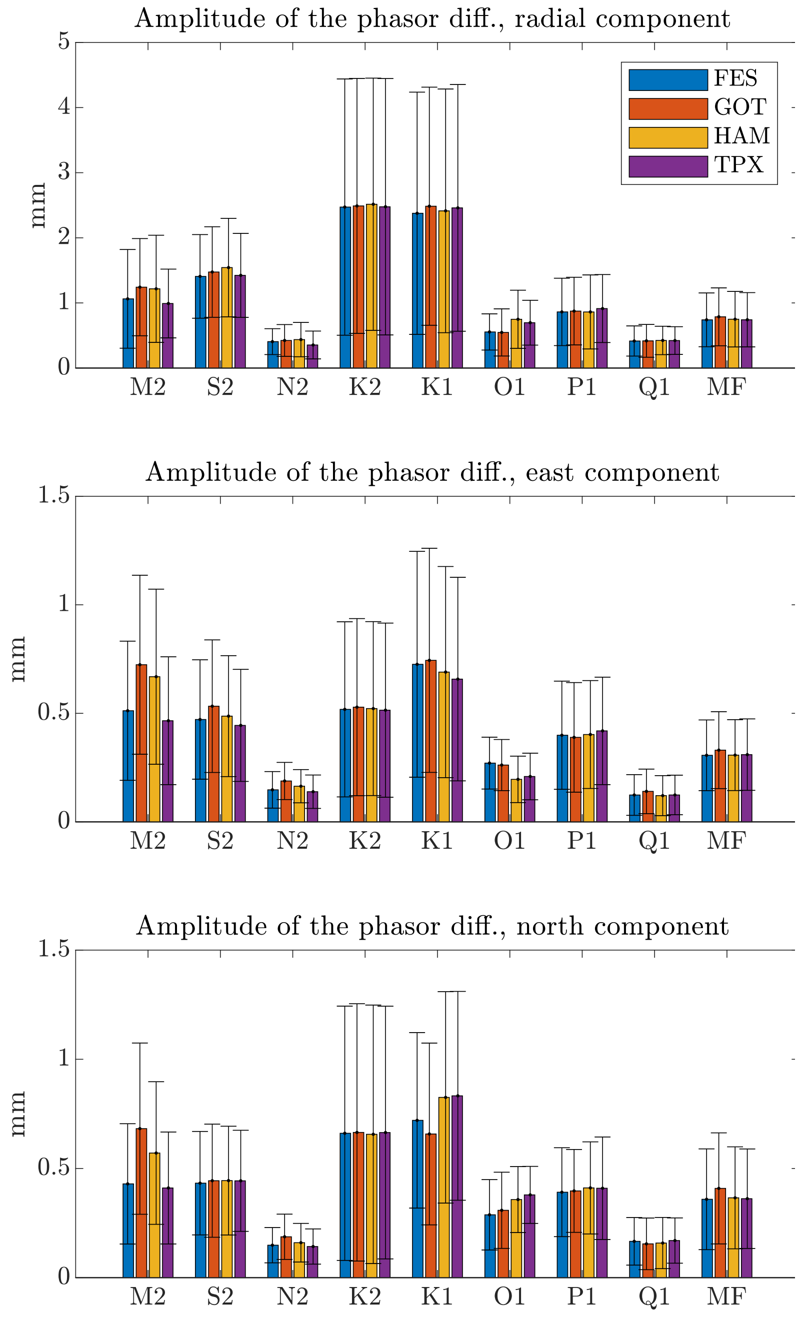

Figure 4.1: *The mean difference for every component and site is displayed for each model, constituent and component. The error bars depict the standard deviation of the compounded difference. As there is great variation in loading amplitude between sites, the standard deviation is quite large. The compounded difference is very similar between models in all constituents and components.*

4.2 Geographical distribution

In this section, the geographical distribution of the difference between models and observations of ocean tidal loading is investigated using the FES2014b model.

Figure 4.2 shows the compounded root mean square (RMS) of the differences in ocean tidal loading amplitude between observation and model FES2014b phasors for each site. This compounded RMS difference contains the three-dimensional amplitude of the difference between models and observation phasors, for the five constituents M_2, N_2, O_1, Q_1 and M_f. It was calculated for each site using the following formula:

$$\text{Compounded RMS diff.} = \sqrt{|\mathrm{M_2\ amp.}|^2 + |\mathrm{N_2\ amp.}|^2 + \ldots}, \tag{4.1}$$

where M_2 amp. is the amplitude of the difference between model and observation phasors for the M_2 constituent for the site. The size of each dot in the figures is inversely proportional to the compounded uncertainty σ_{amp} of the observed amplitude for that site.

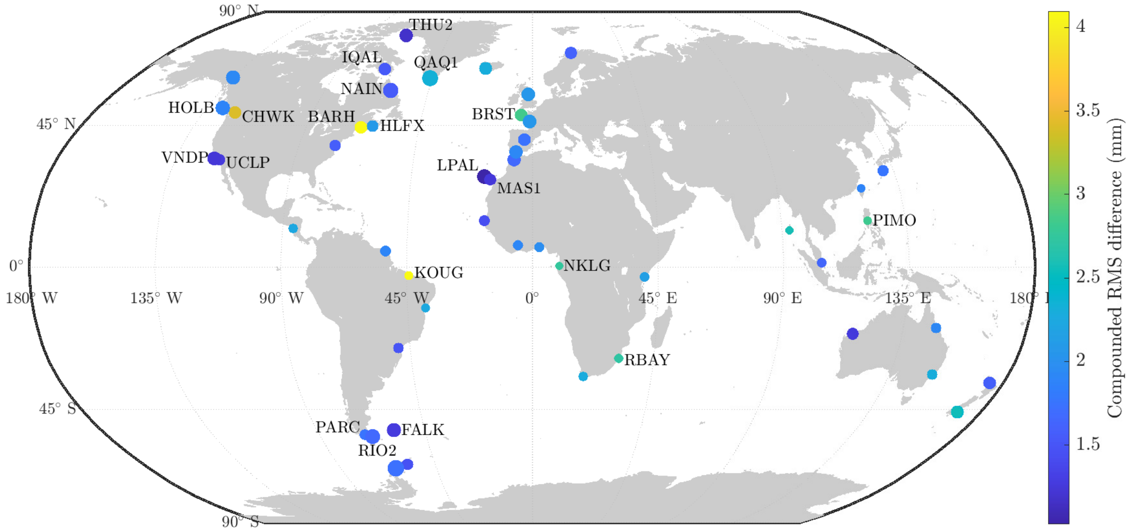

Figure 4.2: *The compounded RMS of the differences in ocean tidal loading between model FES2014b and observations for the* M_2, N_2, O_1, Q_1 *and* M_f *constituents. The size of the dot at each site is inversely proportional to the uncertainty of the observed amplitude for that site.*

The compounded RMS difference between FES2014b and observations varies between sites, and ranges between roughly 1 mm and 4 mm. The mean compounded uncertainty is 0.97 mm. While there are some areas (e.g. western Europe) where the compounded RMS difference is generally a little bit larger (~2-2.5 mm), the compounded uncertainty is too large for a clear, general pattern to be apparent. There are however individual sites where the difference is large ($\geq$ 3 mm). These sites are BRST, NKLG, PIMO, RBAY ($\sim$ 3 mm), CHWK ($\sim$ 3.5 mm) and BARH, KOUG ($\sim$ 4 mm).

Many of these sites are located in areas where the M_2 ocean tide amplitude is especially large; BRST, BARH, CHWK, KOUG, and to a lesser degree RBAY. However, in some areas where M_2 is large, the compounded RMS differences are generally lower; the most pronounced examples are the Labrador sea (IQAL, NAIN, QAQ1, THU2) and southern South America (FALK, PARC, RIO2). Similarly, some of the mentioned sites are located in shallow ocean areas, while the in this context important Patagonian shelf contains none of these sites. It should also be noted that in all of the above mentioned sites except NKLG, the GNSS receiver is mounted on a building (see Section A for a list of all sites and classifications of the monuments). This is discouraged in the IGS guidelines [44].

A few other sites are conspicuous: First is the PIMO site; it has a larger compounded RMS difference ($\sim$ 3 mm), and is located in an area where the M_2 ocean tide amplitude is larger to the east and smaller to the west of the Islands. Second are the two pairs of sites BARH/HLFX and CHWK/HOLB. The CHWK and HOLB sites are located close to each other, and the compounded differences at these rather close sites differ noticeably ($\sim$ 3 mm and $\sim$ 2 mm) respectively, compared to e.g. the VNDP and UCLP stations further south on the same coastline. This is true also for the BARH/HLFX pair ($\sim$ 4 mm and $\sim$ 2 mm, respectively). In the CHWK/HOLB pair, the CHWK site is located noticeably further inland than the HOLB site. In the BARH/HLFX pair, both sites are close to the coast, although BARH is located in a bay.

The compounded uncertainty varies a lot between sites. There is some tendency towards larger uncertainties near the equator, but not a conclusive pattern.

4.3 Differences between model and observations in the loading constituents

This section examines the difference between model and observations in the different constituents; the focus is on the radial component only, as this component is more likely to contain all effects that also affect the horizontal components, but with a better signal to noise ratio in observations. Like the previous section, this section focuses on the difference between the FES2014b model and observations, as the general results are very similar between models.

Figure 4.3 shows the amplitude of the difference between the FES2014b model and observation phasors of ocean tidal loading for the radial component, for the nine constituents considered in this report. The difference between model and observations is between 0 mm and 10 mm, but varies greatly between constituents. For the N_2, O_1 and Q_1 constituents, the difference is small; between 0 mm and 2 mm. The differences are only a little bit larger in the M_f constituent (0-2.5 mm). In P_1 and M_2 the difference between model and observations is similar to that of M_f, but there are several cases that reach 3 mm and 4 mm differences. Similar results are seen in S_2, but with more cases in the upper bounds of this interval. Finally there are the K_1 and K_2 constituents, where the difference between model and observations is quite a bit larger; while the majority of sites have differences between 0 mm and

5 mm, many of the sites are in the upper bounds on this interval, and in some cases upwards of 5 mm, up to 10 mm.

To take into account the uncertainty of the observations (σ_{amp}), histograms of the absolute difference between model and observations for the radial components are shown in Figure 4.4. Here, results are similar in the N_2, O_1, Q_1 and M_f constituents, which show the lowest absolute uncertainty (0-$5 \cdot \sigma_{\text{amp}}$). The absolute difference is larger in P_1 (0-$7 \cdot \sigma_{\text{amp}}$). For M_2, the absolute difference is quite a bit larger than in the previously mentioned constituents; in most sites the absolute difference is between $0 \cdot \sigma_{\text{amp}}$ and $10 \cdot \sigma_{\text{amp}}$, with a few cases between $10 \cdot \sigma_{\text{amp}}$ and $20 \cdot \sigma_{\text{amp}}$. The results in S_2 are similar; the absolute difference is between $1 \cdot \sigma_{\text{amp}}$ and $12 \cdot \sigma_{\text{amp}}$, with many cases in the upper bounds of this interval. In K_1 and K_2 the absolute difference between model and observations is very large, coming close to $30 \cdot \sigma_{\text{amp}}$ in a few sites, though the majority of cases are below $20 \cdot \sigma_{\text{amp}}$.

Looking at the difference between model and observations relative to the model amplitude however (Figure 4.5), the results are a bit different. The relative difference is small for M_2, N_2 and O_1, a bit larger in many cases of S_2, and larger still in the remaining constituents. As the model has a limited accuracy, one might expect the relative difference in the low amplitude constituents to be larger than in the high amplitude constituents. Indeed, the low amplitude constituents show a larger relative difference. However, in the high amplitude constituents the relative difference is low in only two constituents (M_2 and O_1), but larger in the third (K_1). In N_2 the relative amplitude is low, while in P_1, which is similar in loading amplitude to N_2, the relative difference is larger.

Figure 4.6 contains histograms of the uncertainty for the radial component of the nine constituents considered in this report. Both the magnitude and distribution of the uncertainty is similar in all constituents and ranges between roughly 0.25 mm and 0.75 mm although slightly larger in a few cases of especially the M_{f} constituent. The uncertainty is ≤ 0.2 mm in 24 % of the sites in M_2, 34 % in O_1 and < 10 % in the other lunar constituents. For the M_2 constituent, the mean and median uncertainties are 0.33 mm and 0.29 mm, respectively.

In the above results, the amplitude of the phasor difference, which contains both the difference in phase and amplitude, was used. Figure 4.7 shows the difference in the loading phase between model and observations. The phase difference is small for M_2, a little larger in some sites for N_2 and O_1, and quite large in many or even the majority of sites in the remaining constituents. It should be noted that a large difference in phase for a low amplitude constituent will not necessarily yield a large amplitude of the phasor difference. In cases where the amplitude of the phasor difference is large but the phase difference is small, the difference between model and observations is caused primarily by differences in the loading amplitude.

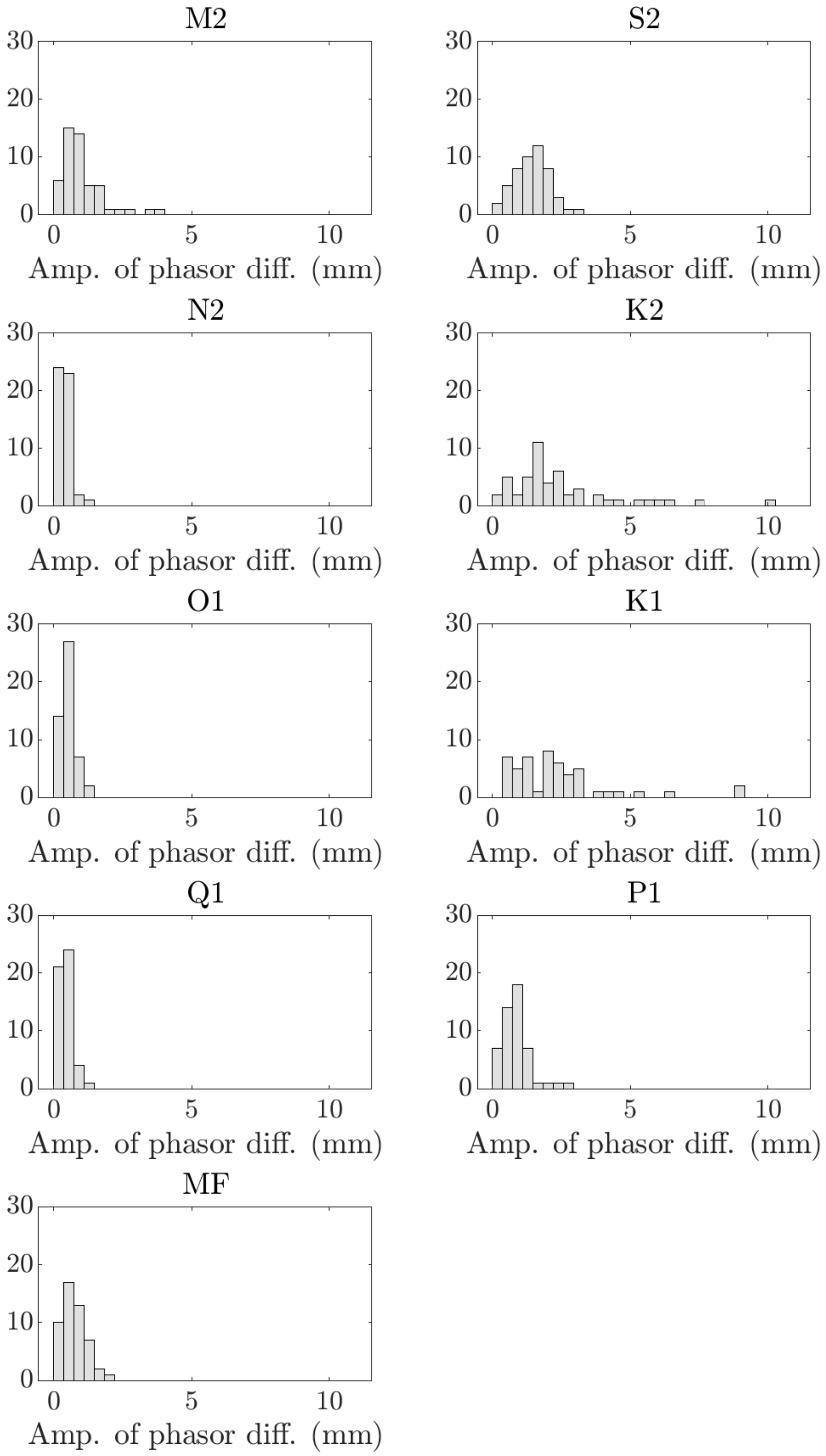

Figure 4.3: *Histograms of the difference between the FES2014b model and observation phasors of ocean tidal loading, for the radial component of each constituent.*

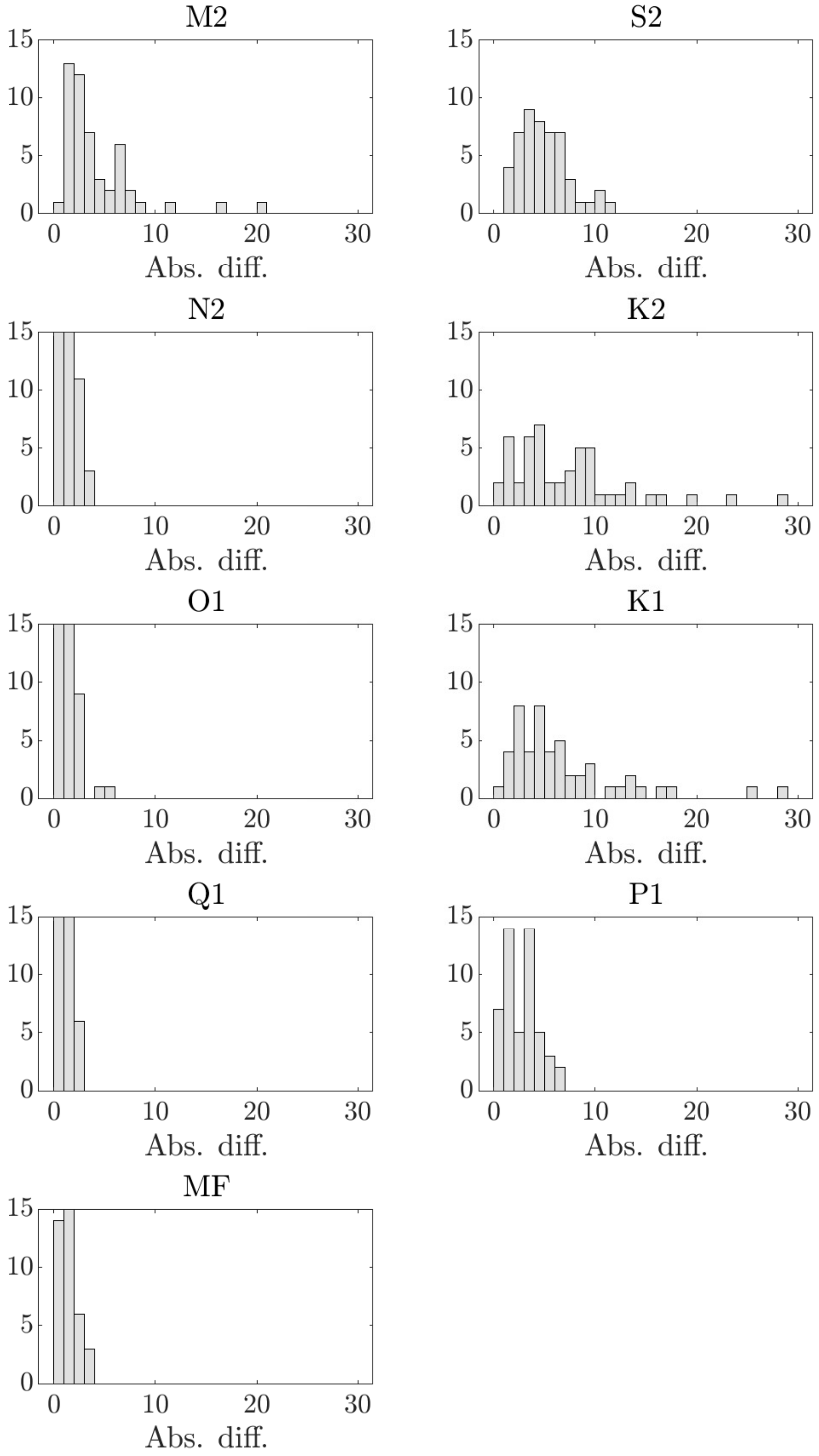

Figure 4.4: *Histograms of the absolute difference in loading amplitude between the FES2014b model and observations of ocean tidal loading, for the radial component of each constituent.*

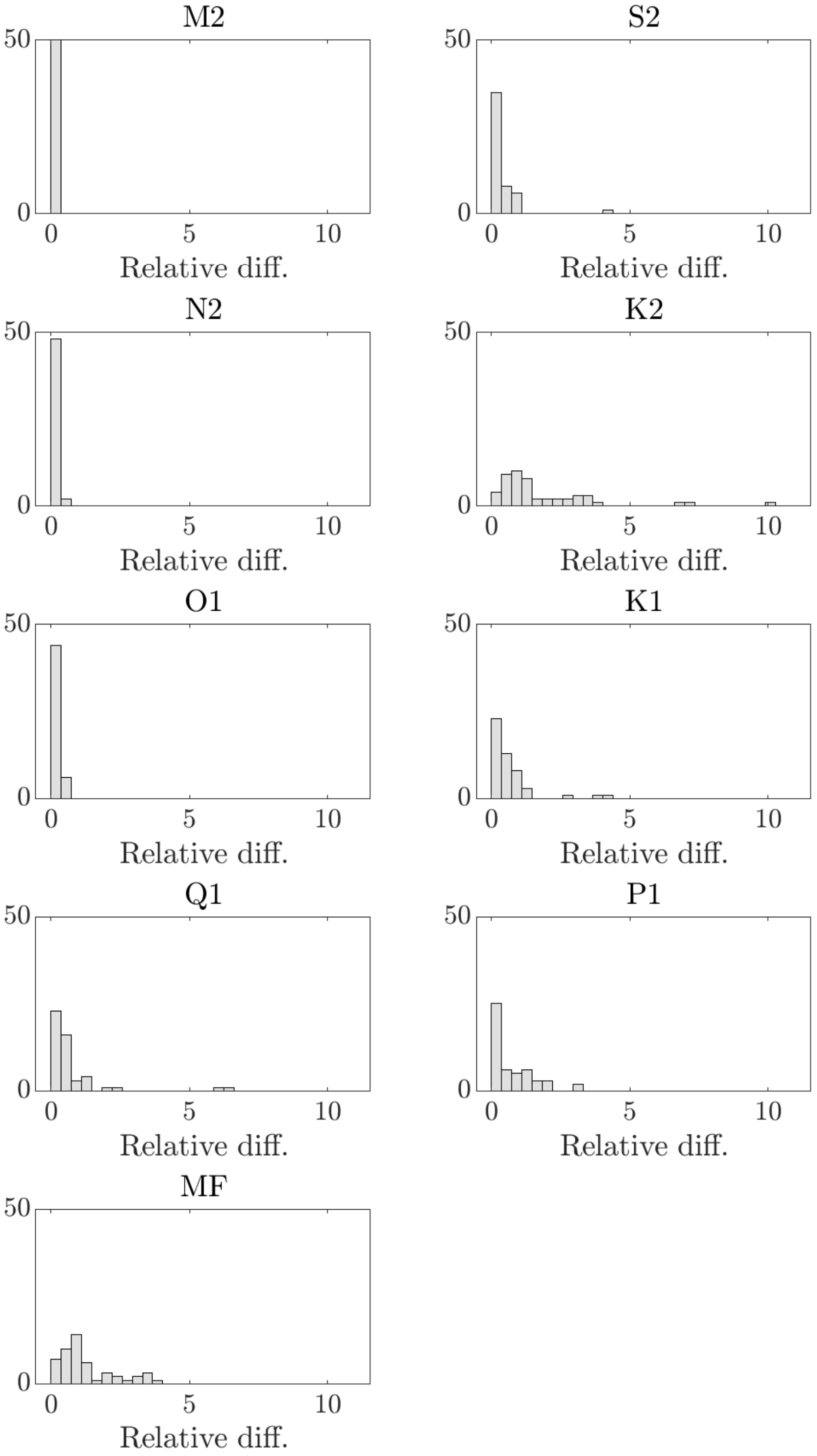

Figure 4.5: *Histograms of the difference in loading amplitude between the FES2014b model and observations of ocean tidal loading, relative to the model amplitude, for the radial component of each constituent.*

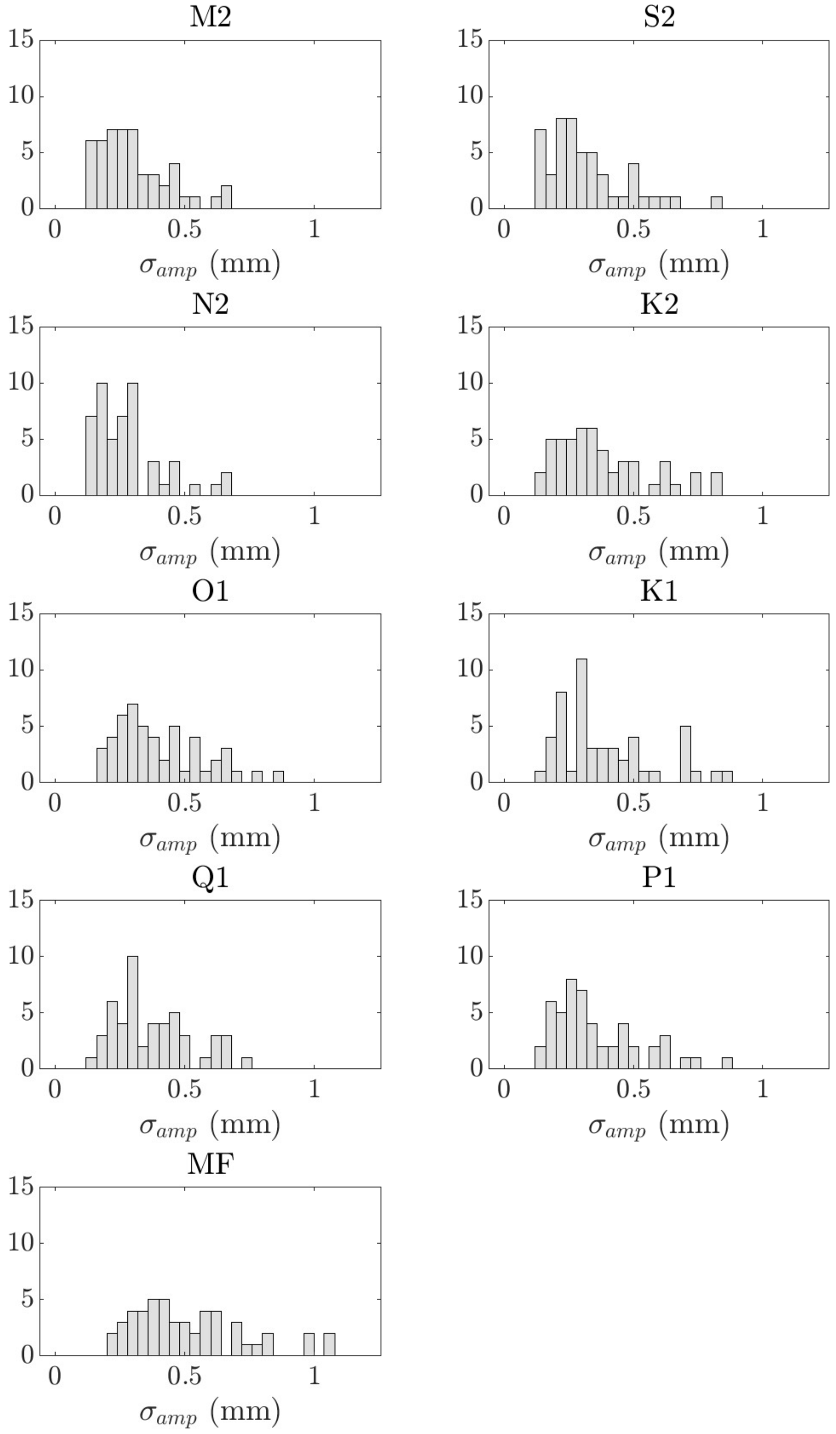

Figure 4.6: *Histograms of the amplitude uncertainty* σ_{amp} *of the observed ocean tidal loading for each constituent.*

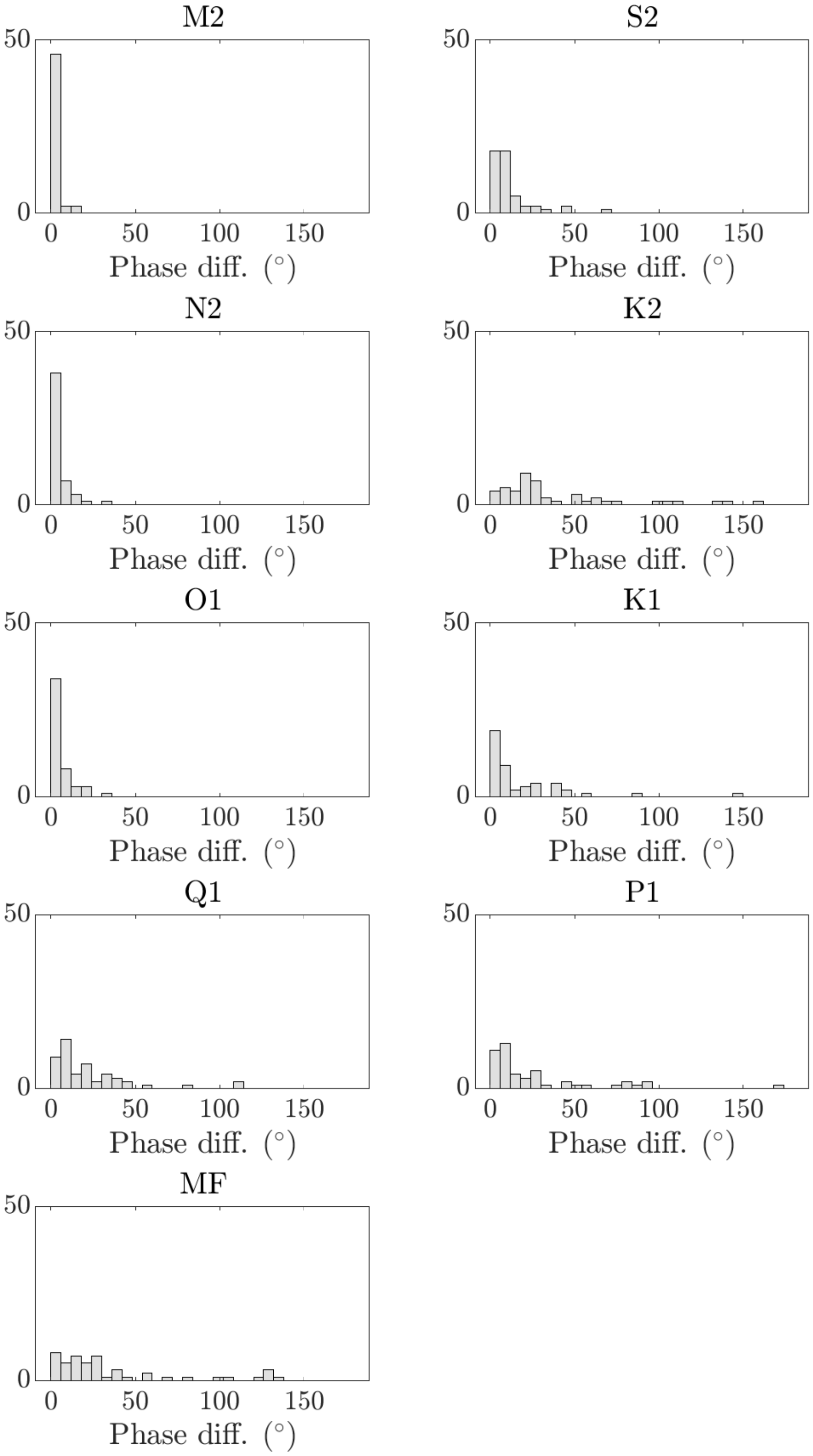

Figure 4.7: *Histograms of the difference in loading phase between the FES2014b model predictions and observations of ocean tidal loading for the radial component of each constituent.*

4.4 Perturbing signals at diurnal and semidiurnal frequencies

Figure 4.8 presents an example of the autocovariance of the residual time series after tidal analysis for the BRST site. There are pronounced spikes at lag 12, and less pronounced spikes at lag 6. This indicates that there remains some periodic signals at these lags, i.e. at 12 h and 24 h periods. (The resolution of the time series is 2 h; a lag of 12 then means a period of $12 \cdot 2$ h= 24 h.) These residual periodic signals are present at different strengths in all sites. The cause of these residual signals is discussed in the following chapter.

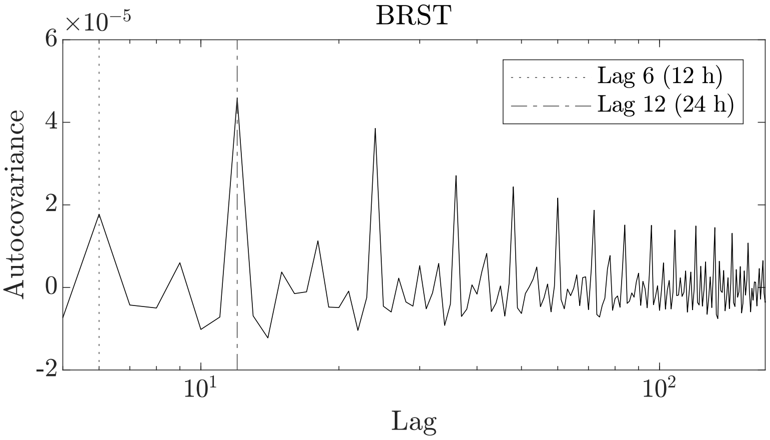

Figure 4.8: *The autocovariance of the residual time series after tidal processing, for the BRST site. Some periodic signals remain, most noticeably at the 24 h period, but also at the 12 h period.*

The S_2, K_1, K_2 and P_1 constituents all have periods very close to 12 h and 24 h (see Table 2.1), while the periods of the other five constituents are further from this. The S_2, K_1, K_2 and P_1 constituents are thus more vulnerable to perturbations from the 12 h and 24 h residual periodic signals. There are more remaining periodic signals present in Figure 4.8, but not at periods which are close to the periods of any of the nine constituents considered in this report.

4.4.1 The S_1 constituent and solar driven perturbations

The S_1 is a small constituent that is normally not included in ocean tidal loading, but is used here to investigate the above mentioned perturbing signals. It has a period of 24.0 h, and is thus very vulnerable to solar driven perturbations. Table 4.1 lists the observed amplitude in the radial component of the S_1 constituent at each site. The amplitude is unexpectedly large in many sites; FES2014b predictions of the S_1 radial loading amplitude are in the sub-millimetre range (mean 0.27 mm, median 0.25 mm) for all sites [45], while the observed amplitude is > 1 mm and up to 6 mm in the majority of the sites. The large observed S_1 amplitudes are indicative of solar driven perturbations.

Table 4.1: *The amplitude of the radial component of S_1 constituent at all 50 sites (in millimetres).*

Site	Amp.	Site	Amp.	Site	Amp.	Site	Amp.	Site	Amp.
MANA	0.165	DUND	1.016	FALK	1.629	MAL2	2.277	LPAL	4.004
SFER	0.198	PBRI	1.101	RABT	1.637	PALM	2.401	PIMO	4.025
NTUS	0.440	BARH	1.109	MORP	1.727	OHI3	2.429	RBAY	4.027
QAQ1	0.621	HLFX	1.117	VNDP	1.757	MAS1	2.622	NKLG	4.040
SYDN	0.634	PARC	1.156	YEBE	1.800	IQAL	2.678	HNUS	4.241
RIO2	0.799	TRO1	1.193	HNPT	2.054	WHIT	2.715	SALU	4.444
AUCK	0.813	THU2	1.208	BRST	2.100	BJCO	2.838	KARR	4.456
GMSD	0.818	OUS2	1.333	LROC	2.118	KOUG	3.372	TCMS	5.116
UCLP	0.860	REYK	1.540	TOW2	2.128	UFPR	3.466	SAVO	5.946
NAIN	0.988	CHWK	1.613	HOLB	2.195	YKRO	3.522	DAKR	6.019

4.5 Pairing of models in the O_1 constituent

In several sites, the model predictions of loading in the O_1 constituent pair up, so that the FES2014b and GOT4.10c predictions are very similar to each other, and the HAMTIDE and TPX09-Atlas predictions in turn being very similar, but differing from the FES2014b/GOT4.10c pair. Figure 4.9 shows two examples of this. The observed and modelled ocean tidal loading is displayed as phasors for the radial (R) component of the WHIT site, and for the north-south (N) component of the YEBE site. The pairing of model predictions can occur in all components, but not necessarily in all components for one site.

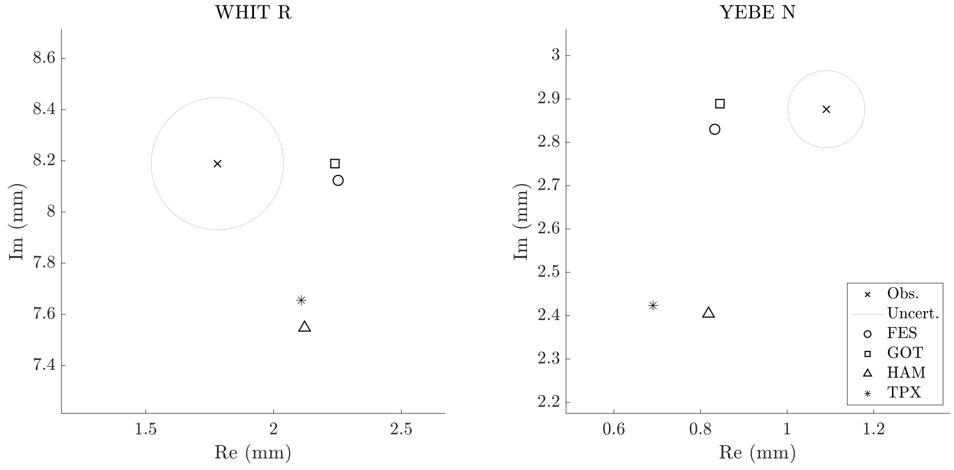

Figure 4.9: *Phasors depicting the observed and modelled amplitude and phase of ocean tidal loading for the O_1 constituent at the WHIT and YEBE sites. The model predictions for the O_1 constituent tend to pair up, with FES2014b and GOT4.10c in one place, and HAMTIDE and TPX09-Atlas in another.*

Figure 4.10 shows the difference between the FES2014b and the GOT4.10c, HAMTIDE and TPX09-Atlas phasors for the M_2 and O_1 constituents. This difference is displayed as phasors for all 50 stations, shown in separate figures for the radial (R), east-west (E) and north-south (N) components. In all components of O_1, the difference between FES2014b and GOT4.10c predictions tends to be smaller than the differences between FES2014b and HAMTIDE/TPX09-Atlas predictions, respectively. This should be compared to M_2, where this pattern is not apparent.

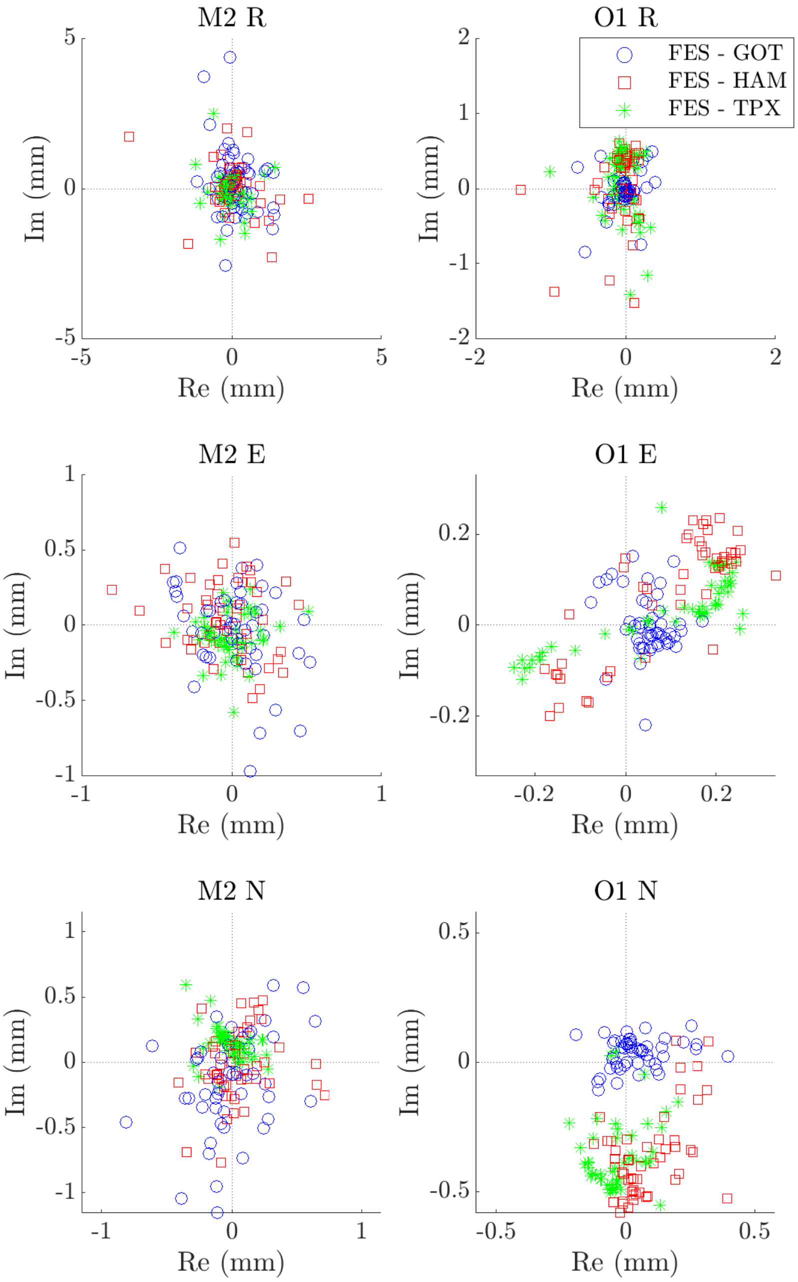

Figure 4.10: *The phasor difference between the FES2014b model predictions of ocean tidal loading for the M_2 and O_1 constituents, and the GOT4.10c, HAMTIDE and TPX09-Atlas model predictions, are shown here for all 50 sites and for each component. The difference between FES2014b and GOT4.10c tends to be smaller than the difference between FES2014b and HAMTIDE or TPX09-Atlas in the O_1 constituent, while no such pattern is seen in M_2.*

5

Discussion

The difference between models and observations of ocean tidal loading is usually up to a few mm, but is dependent on the constituent. The lowest difference was seen in the lunar constituents N_2, O_1 and Q_1 and, when taking into account the uncertainty, M_f. In the last lunar constituent, M_2, the difference between model and observations was larger, however. The difference was also larger in all the solar constituents (S_2, K_1, K_2 and P_1).

5.1 Geographical distribution

There is no clear general pattern in the geographical distribution of the compounded RMS difference between models and observations of ocean tidal loading. Large differences are expected in areas where the ocean tide amplitude (especially the M_2 tide) is large, in shallow ocean areas and near complex coastlines [9]. There are individual sites in such areas that show a large compounded RMS difference, but in other such areas, e.g. the Patagonian shelf, the compounded RMS difference is lower. The lack of a clear geographical pattern is not altogether a surprise, as the sites were chosen to be in locations where the M_2 and O_1 tides are high in amplitude, and thus all sites are in areas where large compounded RMS differences are expected. Also, to properly identify global geographical patterns, many sites distributed evenly over the Earth would be needed. As the majority of GNSS stations are located on land, this is presently unfeasible.

While many sites with larger compounded RMS differences (≥ 3 mm) e.g. BRST are located in the aforementioned areas with large M_2 amplitudes, there are a few that stand out. First is the PIMO site, where the M_2 tide amplitude differs between two close together, opposite coastlines. It is not unlikely that such conditions cause problems in ocean tidal loading models. Additionally, this is in a shallow ocean area, with many islands resulting in a complex coastline, which could exacerbate the problem.

Second is the two pairs of sites: CHWK/HOLB and BARH/HLFX. The two sites in each pair are located near each other, but have quite different compounded RMS differences. Both pairs are located in areas where the M_2 ocean tide is large, but so is the pair of sites LPAL/MAS1, and they show very similar compounded RMS differences. In the case of BARH/HLFX, the BARH site is located in a bay, while the HLFX site is not. This could explain the larger compounded RMS difference in BARH, as the shape of the coastline at BARH could have a negative effect on the ocean models used in ocean tidal loading. In the case of CHWK/HOLB, the CHWK site with the larger compounded RMS difference is located further inland than the HOLB site. According to [46], the depth to which the structure of the Earth's crust affects ocean tidal loading increases with the distance to large loads. It is possible then that since the CHWK site is located more inland, i.e. further from the load, the model of the Earth's structure used in calculating loading models has an adverse effect on the loading model here. This could also be an indication that GNSS measurements of the type carried out in this report are sensitive enough to be useful in testing or constraining Earth models. This is discussed further in Section 5.4.

5.2 The S_2, K_1, K_2 and P_1 constituents

The difference between models and observations of ocean loading is especially large in the solar constituents (S_2, K_1, K_2 and P_1). This is most likely caused by the remaining periodic signals in the time series, shown in Section 4.4. Two of these remaining signals have frequencies very close to the frequencies of the solar constituents, and thus they can disturb the desired signals. The problem in these constituents is then in the observations. The reason for these periodic signals is discussed later in this chapter.

5.3 The M_2 constituent

The difference between models and observations of ocean tidal loading were relatively large in the M_2 constituent, especially when taking into account the uncertainty of observations. As the differences were smaller in the other lunar constituents, this might be a bit surprising. However, M_2 is by far the highest amplitude constituent, and thus the difference is still small, relative to the total amplitude of the constituent. According to [47], the standard deviation in the radial component of M_2 can be expected to be as large as 5 mm or more in some areas; thus differences between models and observations of this magnitude can be expected [7].

Unlike the Sun, the Moon exerts little influence on observable tidal phenomena apart from the gravitational pull, which means the level of perturbations is lower in the lunar constituents. Thus, it is perhaps more reasonable to assume that the larger differences between models and observations in M_2 are model related. This is in agreement with the above statement of larger standard deviations in models of the M_2 constituent.

5.4 Phase vs. amplitude differences

Ocean tidal loading is characterised by an amplitude and a phase in both models and observations. The difference between models and observations can thus be due to differences in either amplitude or phase, or both. In the lunar constituents, the phase difference between models and observations were low for the high amplitude constituents, while increasing with decreasing loading amplitude. This is not entirely a surprise, as phase differences will have less effect on the total difference in low amplitude tides.

Whether the difference between models and observation is due to differences in amplitude or phase could provide a clue to the cause of the difference. As the Earth's response to a load is assumed to be perfectly elastic (in the time frames of the tides in this report), the phase is not affected by the structure of the Earth, but the amplitude is [12, 46]. In ocean tidal loading models the Earth is assumed to be spherically symmetric. Thus in e.g. M_2, where the difference between models and observations is large and mostly due to amplitude differences, this could be related to problems in the loading models relating to the assumptions made about the Earth's structure (see Section 2.1.1).

If GNSS observations of ocean tidal loading are sensitive to the Earth's structure, they could be useful in testing or constraining Earth models. Indeed, this possibility is suggested in [42], and in 2017, GNSS observations of Earth body tides were used to infer limitations on the structure of the so-called large low-shear-velocity provinces in the interior of the Earth [48]. It is clear this is a possibility that warrants attention.

5.5 Model differences

In general, similar results were seen in all models (FES2014b, GOT4.10c. HAMTIDE and TPX09-Atlas). Except for the pairing of models in O_1, any differences between models were local to specific sites. None of the models consistently performed better than the others.

Regarding the pairing of model predictions that occurred in the O_1 constituent, there is no clear explanation. It could however point to some systematicity in ocean tidal loading models, which warrants examination.

5.6 The quality of observations

The spectral resolution of observations is proportional to the number of samples, N. This is important to consider when choosing the length of the time series for tidal analysis, as too low spectral resolution will prevent the tidal analysis software (*urtapt*) from distinguishing between signals with similar frequencies, such as S_1, K_1 and P_1. For these particular constituents, *urtapt* requires at least one year of data.

The length of the time series also affects the uncertainty, which is proportional to $\frac{1}{\sqrt{\mathrm{N}}}$. A longer time series is thus beneficial to both the uncertainty and the spectral resolution. However, the length of the time series is limited by the GNSS data processing time. [7] recommend 4 years of data with 70 % data availability (= 2.8 y in total), which should yield uncertainties around 0.2 mm. As the availability of data was higher in the sites and dates used in this report, observations of ocean tidal loading described were carried out using 3 year long time series. This yielded a high enough spectral resolution to distinguish between the constituents, and an uncertainty that is ≤ 0.5 mm in most cases. As the length of the time series was the same for all sites in this study, any differences relating to the number of samples in each site were avoided. In studies including more sites, certain GNSS stations might require even longer time series to mitigate local problems.

The uncertainty was ≤ 0.2 mm in many cases, but not a majority (24 % of the sites in M2, 34 % in O1 and < 10 % in the other lunar constituents). This shows that such low uncertainties are indeed achievable, though this project did not succeed in doing so as reliably as suggested by [7]. The uncertainties (e.g. for M_2: mean 0.33 mm, median 0.29 mm) are usually smaller than the difference between models and observations, and thus they are low enough that the observations carried out can consistently be used to evaluate ocean tidal loading models (of the lunar constituents; see Section 5.6.2).

The geographical investigation into the differences between models and observations of ocean tidal loading yielded indications that the GNSS station monument has an effect on observations, as monuments located on buildings are over-represented in the sites with the largest model-observation differences. Indeed, the IGS discourages the use of such monuments [44], as buildings are less stable than a monument situated on/in rock/sediment. (Appendix A contains a list of the monument classification for each site.) The location-specific conditions could also lead to problems with multipath, which primarily affects the K_1 (and to a lesser degree, K_2) constituent. This is something that should be considered when selecting sites for observations of ocean tidal loading, in addition to the availability of long time series.

5.6.1 GNSS observations

While a detailed investigation into any artefacts in the GNSS data is beyond the scope of this project, a few things must be mentioned. First, there is the subject of the models used in processing of GNSS data to remove effects of e.g. geophysical phenomena. This project investigates inaccuracies in ocean tidal loading models, and it is reasonable to assume there might be similar inaccuracies in the other models used (e.g. Earth tide models). These errors will of course affect the results.

Second; in this project, ocean tidal loading effects were not removed in the GNSS data processing (since that is what is measured). The absence of ocean tidal loading models will not just affect the coordinate estimation (where ocean tidal loading effects are desired) however, but also the estimation of clock parameters, zenith tropospheric delay and phase ambiguity [49] (see Section 3.2). Additionally, even though ocean tidal loading models were not used in the GNSS data processing in this project, they still affect the results indirectly. This is because ocean tidal loading models are used in the calculations of orbit and clock parameters (provided by the NASA Jet Propulsion Laboratory), and these parameters are used in the data processing. The orbit and clock parameters can also be affected by local problems at the GNSS stations used for estimation of said parameters.

Third, there is the matter of effects that were not taken into account in the processing of GNSS data. The tropospheric gradient was not estimated (see Appendix B), as the effect on the noise level of the resulting time series was deemed negligible. However, it is possible this might still have affected the results. There is also the effect of atmospheric loading on GNSS observations, which is commonly not included in the data processing, and thus will remain in the time series. This is also true for other effects that are captured by the GNSS measurements.

The effect of all these problems is difficult to quantify, but it is clear that GNSS observations do contain errors that the user must bear in mind. The GNSS observations made do not only contain ocean tidal loading, but also any and all other effects and errors that are captured by the GNSS measurements.

5.6.2 Perturbing signals at diurnal and semidiurnal frequencies

The perturbation from remaining periodic signals at diurnal and semidiurnal frequencies in the time series is problematic. As this effect is seen at different strengths in all sites, it is unlikely to be a problem of multipath signals in the GNSS stations (although multipath could be present in some sites, contributing to the especially large differences in K_1 and K_2). (Multipath signals are signals from GNSS satellites that are reflected at ground level before reaching the GNSS stations, instead of travelling directly to the station from the satellite.) The unexpectedly large amplitudes in the S_1 constituent indicates that this is a solar driven perturbation. A possible cause of the remaining signals is then solar irradiance. This can cause materials in the GNSS station to expand and contract periodically, and these slight movements will be detected by high accuracy GNSS measurements. Thus, even though the materials used in the GNSS equipment will be similar in all sites, the type of monument used for the GNSS station might affect the results.

With the presence of perturbing signals affecting the solar constituents (S_2, K_1, K_2 and P_1), the observations of these constituents carried out in this project are likely not good enough that comparisons with models of ocean tidal loading are useful. Thus, the results regarding the difference between models and observations in the S_2, K_1, K_2 and P_1 constituents in this report should be regarded with some scepticism.

6

Conclusion

Ocean tidal loading has been observed at 50 worldwide sites. The observations were carried out using GNSS, and the amplitudes and phases of loading effects at each site were extracted using a tidal analysis software. Model predictions of ocean tidal loading at the 50 sites were acquired, based on four different ocean tide models (FES2014b, TPX09-Atlas, HAMTIDE and GOT4.10c). The differences between observations and models were then investigated.

The general results were similar between models, and there is no model that is better overall. The lowest differences between models and observations were 0-2 mm (in the lunar constituents, except M_2). This is probably as good as can be expected at present, as previous studies have shown that the differences between model predictions are typically 1-2 mm.

The difference between models and observations were noticeably larger in the solar constituents than in the lunar constituents (except M_2). This is due to issues with obtaining accurate observations of ocean tidal loading in the solar constituents, and is a cause for concern. The problem has been identified as perturbing signals of most likely solar origin, probably solar irradiance. There is also the possibility of multipath errors being present in some sites, affecting the K_1 and K_2 constituents. An attempt was made to account for the perturbing signals by treating them as additional tides in the tidal analysis, but without success.

No general geographical patterns were apparent. This is at least in part due to the choice of sites; since the sites are in areas where the M_2 and O_1 amplitudes are large, they are in locations where the models and observations are likely to disagree. The limited amount of sites is also a factor, and as the majority of GNSS stations are on land, it is presently impossible to measure loading effects in many parts of the world.

It has been shown that GNSS observations of ocean tidal loading spanning three years are accurate enough that they can reliably be used to evaluate ocean tidal loading models. Some problems remain: solar driven perturbations negatively affect observations in some constituents, and local effects such as multipath and monument stability complicate the process of acquiring time series of sufficient length and quality.

The greater difference in an inland site compared to nearby coastal sites could suggest that some problems in models might stem from the Earth model used. The generally low phase differences coupled with larger amplitude differences could also indicate a relation to the Earth's structure. The concept of using GNSS observations of ocean tidal loading to investigate the Earth's structure has been suggested previously, and judging from the results of this project, is a concept that deserves investigation. This also sparks the question of whether ocean tidal loading predictions could be improved with adjustments to the Earth models used. Although predictions of tide loading displacements are limited primarily by the accuracy in the ocean tide models used, as observation techniques get more accurate, the Earth's structure might need more consideration.

Looking forward, the process of tidal analysis of GNSS time series needs to be adjusted to reduce the effect of solar driven perturbations. The possibility of using observations of ocean tidal loading to examine the Earth's structure should be investigated. It would also be of interest to examine if modification of the Earth model could improve ocean tidal loading models.

Bibliography

[1] *Ocean tide loading explained.* Online. Accessed: 2020-02-03. N.D. URL: `http://holt.oso.chalmers.se/loading/loadingprimer.html`.

[2] ESA Navipedia. *Ocean loading.* Online. Accessed: 2020-02-03. 2017-01. URL: `https://gssc.esa.int/navipedia/index.php/Ocean_loading`.

[3] M. Ekman. “A concise history of the theories of tides, precession-nutation and polar motion (from antiquity to 1950)”. In: *Surveys in Geophysics* 14.6 (1993), pp. 585–617.

[4] H.-G. Scherneck, M.S. Bos, and R.M.S. Fernandes. “Ocean tide loading - where we are standing”. In: *Proceedings 23d Working Meeting of the European Very Long Baseline Interferometry Group for Geodesy and Astrometry.* Ed. by R. Haas and G. Elgered. EVGA. 2017.

[5] H.-G. Scherneck, J.M. Johansson, and F.H. Webb. “Ocean loading tides in GPS and rapid variations of the frame origin”. In: *Geodesy Beyond 2000.* Heidelberg: Springer-Verlag Berlin, 2000, pp. 32–40.

[6] I.D. Thomas and P.J. Clarke. “A comparison of GPS, VLBI and model estimates of ocean tide loading displacements”. In: *Journal of Geodesy* 81.5 (2007), pp. 359–368.

[7] N.T. Penna et al. “Ocean tide loading displacements in western Europe: 1. Validation of kinematic GPS estimates”. In: *Journal of Geophysical Research: Solid Earth* 120.9 (2015), pp. 6523–6539.

[8] C. Horellou. *maree haute/maree basse.* Pers. comm. Photographs. 2020-05.

[9] N.T. Penna et al. “Assessing the accuracy of predicted ocean tide loading displacement values”. In: *Journal of Geodesy* 82.12 (2008), pp. 893–907.

[10] G. Petit and B. Luzum. *IERS Conventions (2010).* Online. IERS Technical Note No. 36. 2010. URL: `https://apps.dtic.mil/dtic/tr/fulltext/u2/a535671.pdf`.

[11] National Oceanic and Atmospheric Administration. *Harmonic Constituents for 9410170, San Diego, San Diego Bay CA.* Online. Accessed: 2020-03-25. N.D. URL: `https://tidesandcurrents.noaa.gov/harcon.html?id=9410170`.

[12] M.S. Bos and H.-G. Scherneck. “Computation of green’s functions for ocean tide loading”. In: *Sciences of Geodesy - II: Innovations and Future Developments* (2013-01), pp. 1–52.

[13] B. Männel et al. “Correcting surface loading at the observation level: impact on global GNSS and VLBI station networks”. In: *Journal of Geodesy* 93.12 (2019), pp. 2003–2017.

[14] W.E. Farrel. “Deformation of the Earth by surface loads”. In: *Reviews of Geophysics* 10.3 (1972), pp. 761–797.

[15] A.M. Dziewonski and D.L. Anderson. “Preliminary reference Earth model”. In: *Physics of the earth and planetary interiors* 25.4 (1981), pp. 297–356.

[16] B. Gutenberg. “Wave velocities at depths between 50 and 600 kilometers”. In: *Bulletin of the Seismological Society of America* 43.3 (1953), pp. 223–232.

[17] K.E. Bullen. *Seismology.* London: Methuen, 1954.

[18] D. Stammer et al. “Accuracy assessment of global barotropic ocean tide models”. In: *Review of Geophysics* 52 (2014), pp. 243–282.

[19] H.-G. Scherneck. *M2 map.* Pers. comm. M2 ocean tidal constituent map. 2020-05. URL: `http://holt.oso.chalmers.se/hgs/4me/OTide/glb-logamp-pha.m2-map.png`.

[20] L. Carrere et al. “FES 2014, a new tidal model on the global ocean with enhanced accuracy in shallow seas and in the Arctic region.” In: *EGU general assembly conference abstracts.* Vol. 17. EGU General Assembly. 2015.

[21] G.D. Egbert and S.Y. Erofeeva. “Efficient inverse modeling of barotropic ocean tides”. In: *Journal of Atmospheric and Oceanic Technology* 19.2 (2002), pp. 183–204.

[22] E. Taguchi, D. Stammer, and W. Zahel. “Inferring deep ocean tidal energy dissipation from the global high-resolution data-assimilative HAMTIDE model”. In: *Journal of Geophysical Research: Oceans* 119.7 (2014), pp. 4573–4592.

[23] R. Ray. *GOT-4.10c.* Developed at NASA-GSFC. 2013.

[24] M.S. Bos and H.-G. Scherneck. *Ocean tide loading provider.* Online. 2011. URL: `http://holt.oso.chalmers.se/loading/index.html`.

[25] J.M. Johansson. *Principles & Signals.* Lecture (powerpoint). 2019-11.

[26] J.M. Johansson. *Receivers, observables and error sources.* Lecture (powerpoint). 2019-11.

[27] B. Hofmann-Wellenhof, H. Lichtenegger, and E. Wasle. *GNSS — Global Navigation Satellite Systems. GPS, GLONASS, Galileo, and more.* Wien: Springer-Verlag, 2008.

[28] Internation GNSS Service. *IGS.* Material downloaded during April 2020. URL: `http://www.igs.org/`.

[29] International Earth Rotation and Reference Systems Service. *IERS.* Online. Accessed: 20-05-25. 2013. URL: `http://www.iers.org/`.

[30] California Institute of Technology NASA Jet Propulsion Laboratory. *GNSS Time Series.* Online. Accessed: 2020-02-28. N.D. URL: `https://sideshow.jpl.nasa.gov/post/series.html`.

[31] Unavco. *GIPSY-OASIS II.* Accessed: 2020-11-02. URL: `https://www.unavco.org/software/data-processing/postprocessing/gipsy/gipsy.html`.

[32] R. Cefalo, J.B. Zieliński, and M. Barbarella. *New Advanced GNSS and 3D Spatial Techniques: Applications to Civil and Environmental Engineering, Geophysics, Architecture, Archeology and Cultural Heritage.* Cham: Springer, 2017.

[33] J.M. Johansson. *GNSS Data Processing.* Lecture (powerpoint). 2019-12.

[34] J.M. Johansson. *GNSS Data Processing (Part 2).* Lecture (powerpoint). 2019-12.

[35] J.M. Johansson. *Highest precision GNSS.* Lecture (powerpoint). 2019-12.

[36] J. Boehm, B. Werl, and H. Schuh. “Troposphere mapping functions for GPS and very long baseline interferometry from European Centre for Medium-Range Weather Forecasts operational analysis data”. In: *Journal of Geophysical Research: Solid Earth* 111.B2 (2006).

[37] California Institute of Technology NASA Jet Propulsion Laboratory. *JPL GPS Products, Final*. Online. Years: 2008-2017 (updated 2018-06-05), 2018 (updated 2019-01-11). 2018. URL: `https://sideshow.jpl.nasa.gov/pub/JPL_GPS_Products/Final/`.

[38] J.M. Wahr. “Deformation induced by polar motion”. In: *Journal of Geophysical Research* 90.B11 (1985), pp. 9363–9368.

[39] G. Blewitt. “Fixed point theorems of GPS carrier phase ambiguity resolution and their application to massive network processing: Ambizap”. In: *Journal of Geophysical Reserach* 113.B12 (2008).

[40] H.-G. Scherneck. *MAIN PROGRAM URTAPT - Tide analysis package*. Online. Accessed: 2020-03-26. N.D. URL: `http://holt.oso.chalmers.se/hgs/hgs.man/urtapt.html`.

[41] H.-G. Scherneck and M. Rajner. “Using a Superconducting Gravimeter in Support of Absolute Gravity Campaigning — A Feasibility Study”. In: *Geophysica* 54.1 (2019), pp. 117–135.

[42] L. Yuan et al. “The tidal displacement field at Earth’s surface determined using global GPS observations”. In: *Journal of Geophysical Research: Solid Earth* 118.B2 (2013), pp. 2618–2632.

[43] SEGAL. *SEGAL improves free ocean tide loading provider*. Online. Accessed: 20-05-25. 2016-11. URL: `http://segal.ubi.pt/segal-improves-free-ocean-tide-loading-provider/`.

[44] International GNSS Service. *Current IGS Site Guidelines*. Online. Accessed: 2020-09-29. URL: `https://kb.igs.org/hc/en-us/articles/202011433-Current-IGS-Site-Guidelines`.

[45] M. Bos. *FES2014b CMC S1*. Pers. comm. Data. 2020-10.

[46] N.T. Penna et al. “Ocean tide loading displacements in western Europe: 2. GPS-observed anelastic dispersion in the asthenosphere”. In: *Journal of Geophysical Research: Solid Earth* 120.9 (2015), pp. 6540–6557.

[47] N.T. Penna, M.A. King, and M.P. Stewart. “GPS height time series: Short-period origins of spurious long-period signals”. In: *Journal of Geophysical Research: Solid Earth* 112.B12 (2007).

[48] H.C.P. Lau et al. “Tidal tomography constrains Earth’s deep-mantle buoyancy”. In: *Nature* 551 (2017), pp. 321–326.

[49] P. Jarlemark et al. “Station calibration of the Swepos network”. In: *Geophysica* 54.1 (2019), pp. 93–105.

A

List of GNSS stations used

Table A.1: *A list of the GNSS stations used in this report, the coordinates of the stations, the years from which data was collected, and the monument type of the GNSS station. The sampling interval for GNSS data collected from the stations is 30 s.*

Station	Latitude	Longitude	Years	Monument
AUCK	-36.60	174.83	2013-2016	2b
BARH	44.40	-68.22	2015-2018	4b
BJCO	6.38	2.45	2015-2018	2b
BRST	48.38	-4.50	2013-2016	4b
CHWK	49.16	-122.01	2014-2017	4b
DAKR	14.72	-17.44	2016-2019	4b
DUND	-45.88	170.60	2013-2016	3c
FALK	-51.69	-57.87	2016-2019	3b
GMSD	30.56	131.06	2008-2011	4b
HLFX	44.68	-63.61	2016-2019	2a
HNPT	38.59	-76.13	2016-2019	3c
HNUS	-34.42	19.22	2011-2014	2a
HOLB	50.64	-128.14	2014-2017	2a
IQAL	63.76	-68.51	2013-2016	2a
KARR	-20.98	117.10	2016-2019	2a
KOUG	5.10	-52.64	2015-2018	4b
LPAL	28.76	-17.89	2013-2016	4b
LROC	46.16	-1.22	2016-2019	4b
MAL2	-3.00	40.19	2013-2016	2b
MANA	12.15	-86.25	2013-2016	2c
MAS1	27.76	-15.63	2016-2019	2b
MORP	55.21	-1.69	2013-2016	2b
NAIN	56.54	-61.69	2011-2014	2b
NKLG	0.35	9.67	2016-2019	3c
NTUS	1.35	103.68	2012.8-2015.8	4b
OHI3	-63.32	-57.90	2016-2019	2a
OUS2	-45.87	170.51	2013-2016	4b
PALM	-64.78	-64.05	2010-2013	3c
PARC	-53.14	-70.88	2016-2019	4b

PBRI	11.64	92.71	2014.3-2017.3	2b
PIMO	14.64	121.08	2016-2019	4a
QAQ1	60.72	-46.05	2016-2019	2c
RABT	34.00	-6.85	2010-2013	4b
RBAY	-28.80	32.08	2008.5-2011.5	5
REYK	64.14	-21.96	2010-2013	4b
RIO2	-53.79	-67.75	2009-2012	2b
SALU	-2.59	-44.21	2011.5-2014.5	2b
SAVO	-12.94	-38.43	2015-2018	4b
SFER	36.46	-6.21	2010-2013	4b
SYDN	-33.78	151.15	2013-2016	2b
TCMS	24.80	120.99	2014-2017	4b
THU2	76.54	-68.83	2016-2019	2b
TOW2	-19.27	147.06	2013-2016	1
TRO1	69.66	18.94	2016-2019	3a
UCLP	34.07	-118.44	2014-2017	4b
UFPR	-25.45	-49.23	2015-2018	2b
WHIT	60.75	-135.22	2014-2017	2a
VNDP	34.56	-120.62	2009-2012	3c
YEBE	40.52	-3.09	2016-2019	4b
YKRO	6.87	-5.24	2014-2017	2c

Monument types:

1. Directly onto rock
2. Concrete/rock/metal pillar/pipe
    (a) On rock
    (b) On sediment, deep foundation
    (c) On sediment, shallow foundation
3. Metal truss
    (a) On rock
    (b) On sediment, deep foundation
    (c) On sediment, shallow foundation
4. On building
    (a) Dedicated structure
    (b) Other
5. Harbour pier

B

Determination of settings for methods

This chapter describes experimental analyses carried out to determine which settings to use in the respective softwares GIPSY-OASIS and *urtapt*, when processing and analysing the observational data for this report. The use of centre of mass motion corrections in the ocean tidal loading models is also explained.

B.1 Determination of the optimal PEF length for *urtapt*

The Prediction Error Filter (PEF) is used to decorrelate the data input into *urtapt*. In order to be effective, the filter needs to be of a certain length. However, the filtered data contain breaks, the length of which increases with the filter length. Therefore it is important to find a balance between these two needs. The optimal filter length is therefore determined using the principle of maximum entropy, by calculating the Akaike Information Criterion (AIC) for each filter length. An example is shown in Figure B.1: the figure contains the calculated AIC for PEF orders 0-300 (a), with an enlargement of PEF orders 0-15 (b). The minimum AIC corresponds to the maximum entropy PEF order, in this case 6.

In the case of this report, there were some issues in determining which filter length to use; the Akaike criterion yielded unexpectedly large filter lengths. This turned out to be caused by interference in the *urtapt* input data at particularly the 1 cyc./day frequency. In order to determine a good filter length without making the breaks in data too large, the effect of several filter lengths on the autocovariance of the input data was analysed. Figure B.2 shows the autocovariance for four different filter lengths (9, 15, 25 and 50) for two stations (HNUS and KOUG). For each station the filter length was chosen to give the lowest autocovariance at lag 12, i.e. 1 cyc./day. Thus, for HNUS the filter length used was 50, while for KOUG the length 9 was used. The interference that caused this problem is discussed in Chapters 4 and 5.

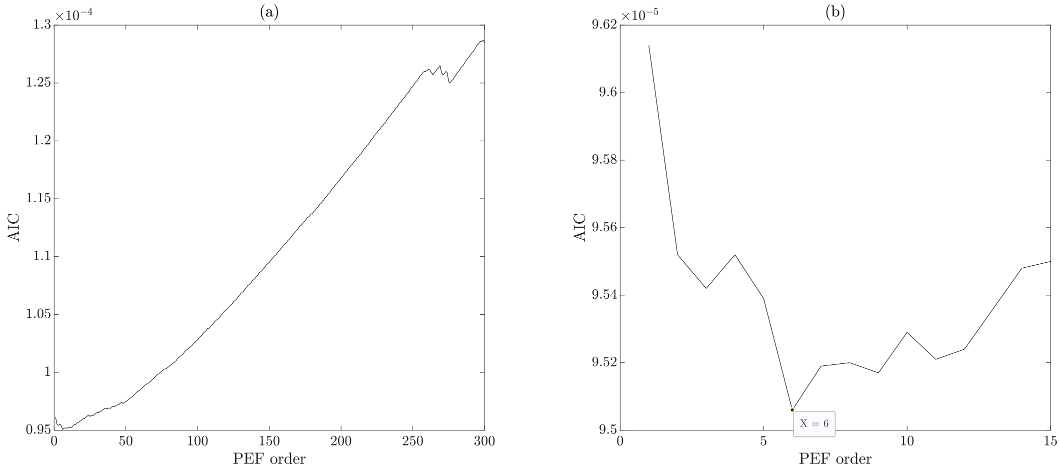

Figure B.1: *The Akaike Information Criterion (AIC) for determining the maximum entropy order of urtapt's PEF. The minimum AIC at PEF order 6 shows that this is the maximum entropy PEF order. Radial component of the ONSA station.*

B.2 Determination of the best time resolution for GNSS data processing

In order to determine which time resolution to use in GIPSY (see Section 3.2), power spectra of the noise from the GIPSY output were created. 1 month of GNSS data from the ONSA station at Onsala space observatory in Sweden was used. The data was processed with GIPSY with different time resolutions: 0.5 h, 1 h and 2 h. The GIPSY processing was performed with and without tropospheric gradient estimation for the 1 h resolution, to analyse the effect of this setting on the noise level.

The ocean tidal loading effects were removed from the time series outut by GIPSY using *urtapt*, and the residual containing the noise was used to create the power spectra in Figure B.3. For each component the noise decreases with the time resolution. The effect of gradient estimation on the noise level is negligible.

B.3 Center of mass correction in ocean tidal loading models

The Ocean tide loading provider from which the ocean tide loading models are acquired contains the option to use centre of mass correction (CMC) when computing the models. This means that the reference frame is centred at the joint mass centre of the solid Earth and the ocean, instead of at the mass centre of the solid Earth. Figure B.4 shows an example of comparisons between models and observations, where the left column is without CMC correction, and the right column is with CMC corrections. The difference between models and observations is smaller for the 'with CMC' case, so the choice was made to use CMC corrections in the model acquisition.

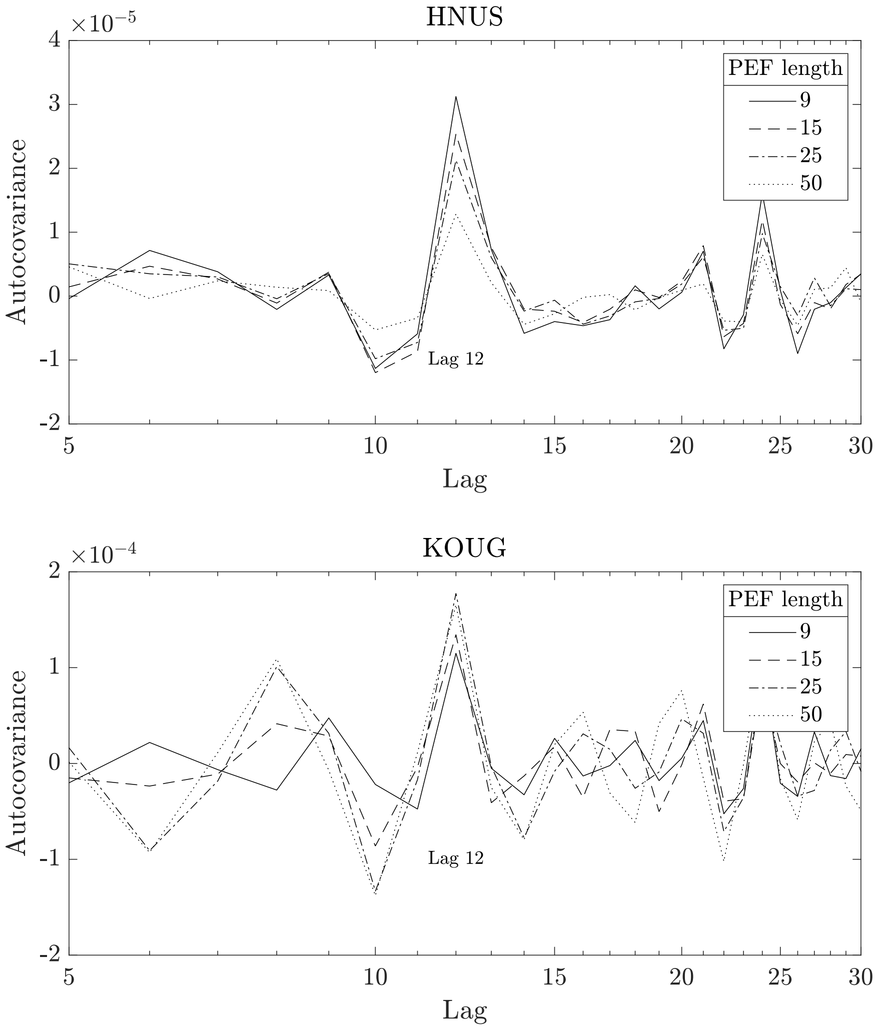

Figure B.2: *The autocovariance of the filtered residuals from the urtapt output yielded by analysing GNSS time series from stations HNUS and KOUG. Four PEF lengths were used: 9, 15, 25 and 50. The autocovariance at lag 12 (1 cyc./day) is lowest at PEF length 50 for HNUS, and 9 for KOUG.*

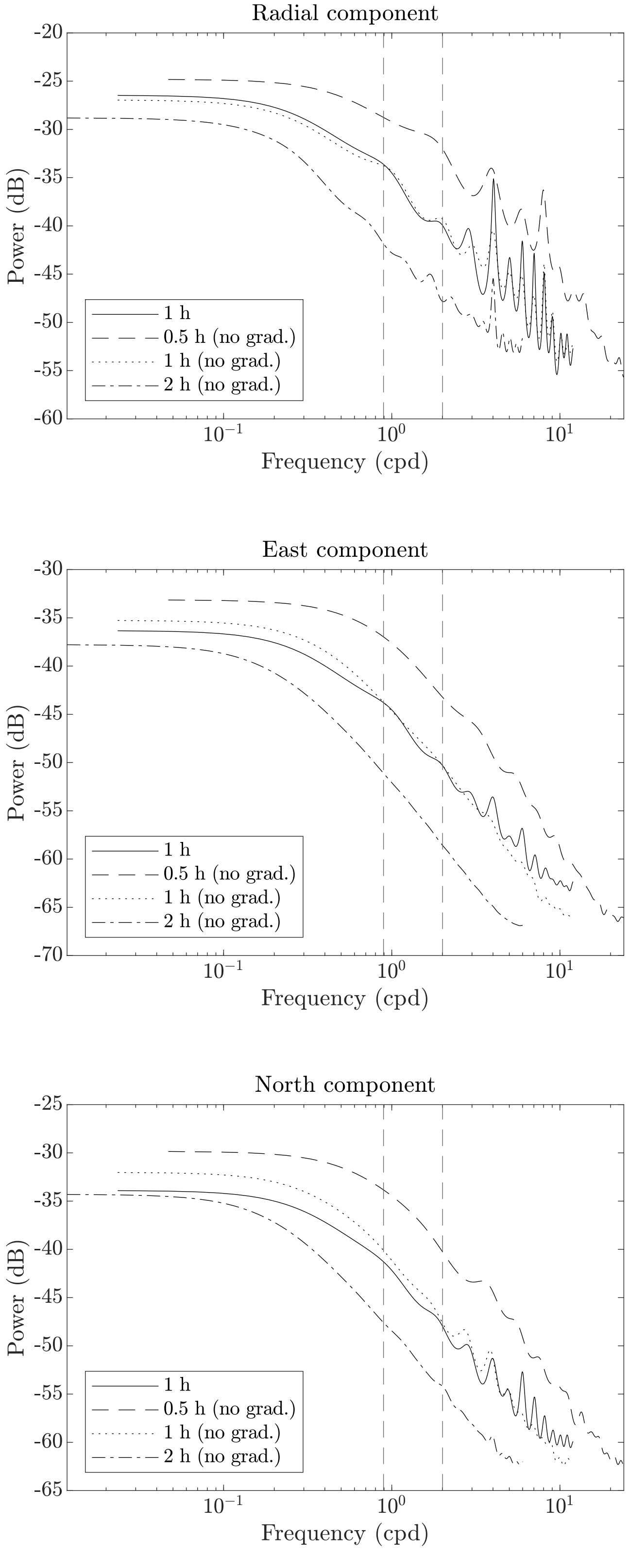

Figure B.3: *The noise level of a GNSS timseries output from GIPSY, for three different time resolutions and for estimation of the tropospheric gradient in GIPSY turned on or off. The noise level is lowest in the relevant frequency span (*$\sim 0.9 - 2$ *cpd) for the 2 h time resolution, and the difference between gradient estimation turned on or off is negligible.*

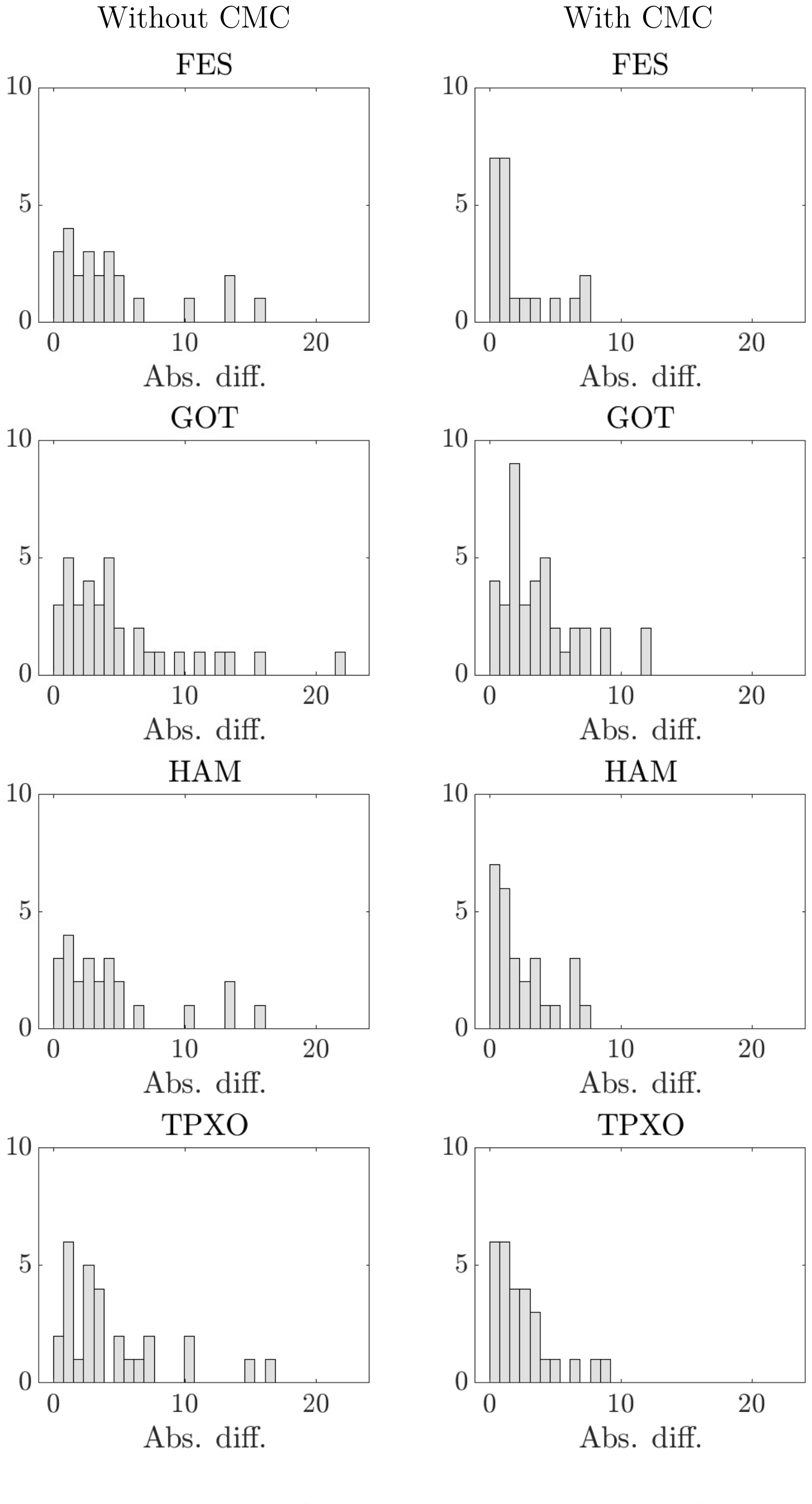

Figure B.4: *The absolute difference between models FES2014b, GOT4.10c, HAMTIDE and TPX09-Atlas, and observations. The left column is without centre of mass corrections, and the right column is with corrections. The difference between models and observations is smaller when corrections are used.*

C

PEF lengths

Table C.1: *The prediction error filter (PEF) lengths used in the tidal analysis with urtapt.*

Station	PEF length	Station	PEF length
AUCK	50	QAQ1	15
BARH	50	RABT	50
BJCO	50	RBAY	50
BRST	50	REYK	50
CHWK	15	RIO2	50
DAKR	50	SALU	50
DUND	50	SAVO	50
FALK	9	SFER	50
GMSD	15	SYDN	50
HLFX	50	TCMS	50
HNPT	50	THU2	50
HNUS	50	TOW2	50
HOLB	15	TRO1	50
IQAL	50	UCLP	50
KARR	50	UFPR	50
KOUG	9	WHIT	50
LPAL	9	VNDP	9
LROC	50	YEBE	15
MAL2	15	YKRO	50
MANA	50		
MAS1	50		
MORP	9		
NAIN	25		
NKLG	25		
NTUS	9		
OHI3	50		
OUS2	50		
PALM	9		
PARC	50		
PBRI	50		
PIMO	50		

D

Ocean tidal loading observation results

Table D.1 contains the observed amplitude and phase of the M_2 and O_1 constituents for all 50 stations. Corresponding data for the other constituents are available from the author upon reasonable request.

Table D.1: *The observed amplitude and phase of the M_2 and O_1 constituents for all 50 stations.*

Site	Tide	Comp.	Amp. (mm)	σ_{amp} (mm)	Phase (°)	σ_{phase} (°)
AUCK	M2	R	28.30	0.2	307.81	0.5
		E	8.67	0.1	196.38	0.4
		N	6.26	0.1	142.69	0.6
	O1	R	1.29	0.3	50.22	14.8
		E	1.42	0.1	298.09	4.9
		N	3.29	0.1	298.09	2.3
BARH	M2	R	15.94	0.2	121.29	0.7
		E	3.35	0.1	293.70	1.0
		N	4.31	0.1	108.41	0.9
	O1	R	4.75	0.3	318.89	3.5
		E	1.80	0.1	157.06	3.8
		N	2.13	0.1	270.95	3.7
BJCO	M2	R	15.19	0.2	74.85	0.9
		E	2.58	0.1	-13.65	2.0
		N	5.25	0.1	87.72	1.1
	O1	R	2.02	0.5	212.10	15.5
		E	0.58	0.2	141.94	16.1
		N	3.11	0.2	269.63	3.8
BRST	M2	R	40.78	0.2	62.34	0.3
		E	7.38	0.1	77.10	0.5
		N	6.65	0.1	133.89	0.7
	O1	R	3.85	0.2	215.00	3.3
		E	1.46	0.1	152.69	5.8
		N	2.70	0.2	287.94	3.3
CHWK	M2	R	7.92	0.3	266.01	2.1
		E	4.50	0.0	256.96	0.5

Table D.1: *The observed amplitude and phase of the M_2 and O_1 constituents for all 50 stations.*

Site	Tide	Comp.	Amp. (mm)	σ_{amp} (mm)	Phase (°)	σ_{phase} (°)
		N	1.78	0.1	74.22	2.4
	O1	R	9.48	0.3	299.50	1.9
		E	2.31	0.1	282.66	1.8
		N	1.93	0.1	255.09	2.8
DAKR	M2	R	13.74	0.4	299.87	1.6
		E	3.89	0.1	300.01	0.8
		N	4.05	0.1	-11.59	0.9
	O1	R	2.75	0.5	287.13	9.7
		E	1.13	0.1	167.39	5.2
		N	3.08	0.1	281.33	2.1
DUND	M2	R	6.82	0.2	81.02	1.9
		E	6.56	0.1	196.51	0.5
		N	7.53	0.1	100.57	0.6
	O1	R	4.02	0.3	8.45	4.4
		E	1.69	0.1	309.50	3.7
		N	3.13	0.1	309.93	2.4
FALK	M2	R	17.19	0.1	248.64	0.5
		E	3.56	0.0	121.34	0.7
		N	1.36	0.1	219.06	2.3
	O1	R	13.60	0.2	118.70	1.0
		E	1.67	0.1	162.06	2.7
		N	1.77	0.1	233.81	3.4
GMSD	M2	R	19.16	0.5	247.75	1.4
		E	3.50	0.1	138.69	1.2
		N	3.27	0.1	210.31	1.6
	O1	R	9.60	0.4	136.35	2.3
		E	3.06	0.1	345.26	1.8
		N	1.41	0.1	259.39	3.7
HLFX	M2	R	14.86	0.3	169.67	1.3
		E	2.46	0.1	44.28	1.3
		N	3.36	0.1	180.89	1.2
	O1	R	4.11	0.3	307.20	4.4
		E	1.64	0.1	156.58	3.8
		N	1.92	0.1	271.80	4.3
HNPT	M2	R	10.86	0.2	192.57	1.0
		E	2.77	0.1	-27.09	1.8
		N	1.06	0.1	147.17	6.0
	O1	R	3.81	0.4	311.97	5.6
		E	1.93	0.2	154.12	4.5
		N	2.55	0.2	260.24	5.0
HNUS	M2	R	25.94	0.2	137.67	0.5
		E	1.03	0.1	141.07	5.6
		N	3.75	0.1	144.30	1.8

Table D.1: *The observed amplitude and phase of the M_2 and O_1 constituents for all 50 stations.*

Site	Tide	Comp.	Amp. (mm)	σ_{amp} (mm)	Phase (°)	σ_{phase} (°)
	O1	R	2.32	0.6	172.72	15.5
		E	0.44	0.2	44.41	30.4
		N	2.82	0.2	242.19	4.6
HOLB	M2	R	27.07	0.1	282.13	0.3
		E	6.89	0.0	264.41	0.4
		N	1.61	0.1	29.78	2.1
	O1	R	14.65	0.2	300.12	0.8
		E	2.61	0.1	284.93	2.4
		N	1.88	0.1	265.31	3.8
IQAL	M2	R	25.05	0.3	196.97	0.6
		E	3.91	0.1	78.27	0.8
		N	7.41	0.1	168.14	0.5
	O1	R	2.63	0.3	307.41	6.9
		E	1.55	0.1	173.30	3.5
		N	0.79	0.1	239.59	7.9
KARR	M2	R	13.20	0.3	127.32	1.3
		E	1.73	0.1	318.24	2.4
		N	4.60	0.1	310.08	1.0
	O1	R	7.70	0.3	19.50	2.3
		E	2.57	0.1	-8.93	3.0
		N	4.08	0.1	254.05	2.0
KOUG	M2	R	25.68	0.2	303.44	0.5
		E	4.54	0.1	138.61	0.8
		N	3.86	0.1	123.44	1.2
	O1	R	3.98	0.4	307.74	6.4
		E	2.28	0.1	154.92	3.1
		N	2.82	0.2	263.58	3.5
LPAL	M2	R	24.25	0.1	141.93	0.3
		E	1.74	0.0	284.82	1.2
		N	4.02	0.0	299.12	0.6
	O1	R	4.09	0.2	255.19	3.5
		E	1.35	0.1	157.71	3.1
		N	3.13	0.1	288.18	1.6
LROC	M2	R	27.91	0.2	79.99	0.3
		E	8.62	0.1	78.09	0.4
		N	3.45	0.1	107.76	1.0
	O1	R	3.10	0.3	225.69	4.7
		E	1.45	0.1	157.85	5.1
		N	2.90	0.1	292.23	2.3
MAL2	M2	R	27.20	0.5	152.29	0.9
		E	4.54	0.1	-2.82	0.9
		N	6.25	0.1	145.59	0.6
	O1	R	5.11	0.5	171.94	6.2

Table D.1: *The observed amplitude and phase of the M_2 and O_1 constituents for all 50 stations.*

Site	Tide	Comp.	Amp. (mm)	σ_{amp} (mm)	Phase (°)	σ_{phase} (°)
		E	1.45	0.1	12.87	5.1
		N	2.71	0.1	259.97	2.8
MANA	M2	R	18.01	0.5	284.70	1.6
		E	2.45	0.1	264.46	1.9
		N	3.03	0.1	291.40	1.9
	O1	R	2.23	0.6	329.26	15.5
		E	1.35	0.2	132.43	7.1
		N	3.01	0.2	257.87	3.6
MAS1	M2	R	23.42	0.3	143.24	0.7
		E	0.99	0.1	254.91	3.5
		N	3.97	0.1	303.38	0.8
	O1	R	3.65	0.4	254.29	5.7
		E	1.25	0.1	167.52	5.7
		N	3.15	0.1	287.15	1.8
MORP	M2	R	14.49	0.2	81.65	0.8
		E	1.99	0.0	302.40	1.4
		N	2.47	0.1	43.69	1.2
	O1	R	1.59	0.2	204.79	8.3
		E	1.64	0.1	160.42	3.6
		N	2.54	0.1	295.91	2.4
NAIN	M2	R	16.35	0.2	215.66	0.6
		E	1.25	0.0	94.26	2.2
		N	3.08	0.1	50.97	1.1
	O1	R	2.48	0.2	323.51	5.0
		E	1.60	0.1	168.51	2.8
		N	1.65	0.1	256.54	3.2
NKLG	M2	R	17.65	0.7	89.88	2.1
		E	4.08	0.1	50.18	1.4
		N	3.92	0.1	124.32	2.0
	O1	R	0.82	0.7	176.24	56.1
		E	0.25	0.2	116.54	62.2
		N	3.11	0.3	270.47	4.8
NTUS	M2	R	4.28	0.5	166.91	6.3
		E	2.40	0.1	-19.99	2.2
		N	1.08	0.1	155.15	5.4
	O1	R	1.76	0.5	10.57	15.0
		E	0.79	0.2	20.86	11.9
		N	3.07	0.2	237.11	3.5
OHI3	M2	R	23.99	0.2	272.70	0.5
		E	1.52	0.1	100.00	2.0
		N	0.37	0.1	128.03	11.5
	O1	R	19.32	0.4	129.70	1.2
		E	1.38	0.1	135.89	4.6

Table D.1: *The observed amplitude and phase of the M_2 and O_1 constituents for all 50 stations.*

Site	Tide	Comp.	Amp. (mm)	σ_{amp} (mm)	Phase (°)	σ_{phase} (°)
		N	2.34	0.1	250.68	3.5
OUS2	M2	R	6.24	0.3	81.31	2.7
		E	6.66	0.1	196.79	0.8
		N	7.25	0.1	100.64	0.9
	O1	R	3.83	0.5	4.80	7.1
		E	1.59	0.2	302.39	6.3
		N	3.45	0.2	313.71	2.9
PALM	M2	R	17.35	0.1	278.65	0.4
		E	1.97	0.0	93.71	1.0
		N	0.31	0.1	132.50	10.8
	O1	R	16.57	0.2	124.85	0.6
		E	1.19	0.1	100.51	3.3
		N	1.54	0.1	267.83	3.7
PARC	M2	R	4.64	0.3	222.09	3.7
		E	3.82	0.1	1.30	1.3
		N	2.62	0.1	289.82	1.6
	O1	R	12.26	0.4	117.63	1.9
		E	1.92	0.2	171.86	6.5
		N	1.08	0.2	246.53	8.1
PBRI	M2	R	16.40	0.6	95.76	2.2
		E	2.03	0.1	326.58	3.2
		N	2.10	0.1	200.06	3.2
	O1	R	1.64	0.7	4.72	25.6
		E	0.88	0.2	308.40	15.6
		N	2.42	0.3	263.30	6.9
PIMO	M2	R	8.41	0.4	227.52	2.5
		E	4.18	0.1	73.63	1.4
		N	3.12	0.1	125.61	2.0
	O1	R	7.24	0.8	68.07	6.7
		E	4.12	0.2	344.53	2.9
		N	3.22	0.2	286.79	3.3
QAQ1	M2	R	16.51	0.1	269.92	0.4
		E	6.04	0.0	222.12	0.4
		N	0.71	0.1	305.16	4.2
	O1	R	0.81	0.2	-9.31	12.0
		E	1.65	0.1	150.59	2.5
		N	1.05	0.1	276.06	5.0
RABT	M2	R	21.64	0.3	114.28	0.8
		E	4.98	0.0	123.12	0.6
		N	3.54	0.1	294.83	1.1
	O1	R	2.54	0.3	253.90	6.5
		E	1.20	0.1	160.22	3.8
		N	2.49	0.1	290.77	2.2

Table D.1: *The observed amplitude and phase of the M_2 and O_1 constituents for all 50 stations.*

Site	Tide	Comp.	Amp. (mm)	σ_{amp} (mm)	Phase (°)	σ_{phase} (°)
RBAY	M2	R	24.88	0.7	134.35	1.5
		E	1.40	0.1	-18.69	3.3
		N	2.99	0.1	125.44	1.9
	O1	R	2.22	0.6	194.99	16.4
		E	0.44	0.1	-4.81	18.3
		N	2.35	0.1	249.75	2.9
REYK	M2	R	20.52	0.3	-1.22	0.7
		E	3.78	0.0	328.74	0.7
		N	5.85	0.1	44.47	0.7
	O1	R	1.35	0.3	142.82	14.5
		E	1.56	0.1	139.72	2.9
		N	1.26	0.1	289.07	5.1
RIO2	M2	R	22.57	0.3	205.38	0.7
		E	6.19	0.1	29.15	0.5
		N	7.01	0.1	328.78	0.5
	O1	R	12.66	0.2	119.85	1.0
		E	1.17	0.1	184.05	3.9
		N	1.16	0.1	246.00	5.0
SALU	M2	R	31.02	0.5	300.14	1.0
		E	4.24	0.1	161.25	1.4
		N	7.86	0.1	117.49	1.0
	O1	R	2.92	0.8	333.77	15.3
		E	1.82	0.2	163.16	5.0
		N	1.70	0.2	258.50	7.4
SAVO	M2	R	24.62	0.4	-24.22	1.0
		E	4.21	0.1	174.31	1.3
		N	3.37	0.1	116.61	1.6
	O1	R	2.12	0.7	37.89	18.7
		E	2.12	0.2	175.59	5.1
		N	2.49	0.2	261.55	3.8
SFER	M2	R	22.41	0.2	111.47	0.6
		E	4.88	0.1	119.04	0.6
		N	1.03	0.1	155.47	4.9
	O1	R	2.23	0.3	244.44	8.4
		E	1.31	0.1	159.47	3.5
		N	2.66	0.1	286.35	2.8
SYDN	M2	R	12.36	0.4	246.68	1.9
		E	4.99	0.1	92.97	0.8
		N	2.40	0.1	130.45	1.5
	O1	R	1.68	0.5	332.61	18.4
		E	2.37	0.1	-11.93	2.9
		N	3.54	0.1	293.80	1.9
TCMS	M2	R	11.50	0.3	141.58	1.6

Table D.1: *The observed amplitude and phase of the M_2 and O_1 constituents for all 50 stations.*

Site	Tide	Comp.	Amp. (mm)	σ_{amp} (mm)	Phase (°)	σ_{phase} (°)
		E	8.16	0.1	74.23	0.8
		N	2.29	0.2	250.35	4.5
	O1	R	7.29	0.7	90.91	5.3
		E	3.42	0.3	342.69	4.4
		N	2.61	0.3	286.61	6.4
THU2	M2	R	10.22	0.2	77.41	1.1
		E	0.71	0.0	12.06	3.1
		N	1.08	0.0	44.91	2.2
	O1	R	4.59	0.3	289.52	3.1
		E	1.40	0.1	183.48	4.4
		N	0.22	0.1	229.65	27.2
TOW2	M2	R	9.75	0.4	211.30	2.2
		E	2.68	0.1	89.03	1.8
		N	1.89	0.1	74.58	2.2
	O1	R	3.49	0.5	133.19	7.8
		E	3.18	0.2	345.49	2.9
		N	3.82	0.2	290.24	2.6
TRO1	M2	R	11.48	0.3	175.22	1.6
		E	1.73	0.0	229.70	1.6
		N	2.86	0.1	14.18	1.2
	O1	R	2.20	0.3	207.89	8.5
		E	1.16	0.1	133.28	4.7
		N	2.21	0.1	317.10	3.3
UCLP	M2	R	5.91	0.3	49.41	3.2
		E	1.29	0.1	233.49	2.8
		N	5.60	0.1	93.38	0.7
	O1	R	11.04	0.4	324.08	2.2
		E	1.82	0.1	304.07	4.1
		N	2.03	0.1	272.15	3.8
UFPR	M2	R	8.66	0.3	316.87	1.7
		E	2.31	0.1	178.57	1.8
		N	3.78	0.1	148.01	1.2
	O1	R	4.24	0.5	101.38	7.1
		E	2.45	0.1	180.44	2.8
		N	2.08	0.2	245.83	4.4
WHIT	M2	R	11.19	0.2	256.00	0.9
		E	3.65	0.0	233.87	0.7
		N	3.07	0.1	265.38	1.1
	O1	R	8.38	0.3	282.27	1.8
		E	1.69	0.1	256.52	3.0
		N	2.49	0.1	252.52	2.8
VNDP	M2	R	8.84	0.2	24.62	1.4
		E	2.15	0.1	261.41	1.4

Table D.1: *The observed amplitude and phase of the M_2 and O_1 constituents for all 50 stations.*

Site	Tide	Comp.	Amp. (mm)	σ_{amp} (mm)	Phase (°)	σ_{phase} (°)
		N	5.41	0.1	95.67	0.6
	O1	R	13.72	0.3	327.44	1.1
		E	2.00	0.1	313.08	2.4
		N	1.62	0.1	284.26	3.2
YEBE	M2	R	13.03	0.2	92.62	1.1
		E	2.65	0.0	98.07	0.9
		N	0.96	0.0	223.76	2.8
	O1	R	1.65	0.3	241.11	12.0
		E	1.41	0.1	149.90	3.1
		N	3.08	0.1	290.77	1.7
YKRO	M2	R	8.69	0.4	42.55	2.7
		E	3.65	0.1	320.03	1.4
		N	3.23	0.1	71.64	1.5
	O1	R	1.56	0.5	252.28	18.2
		E	0.63	0.1	153.72	12.9
		N	3.08	0.2	274.37	3.0